New Insights into the Rift-to-Drift Process of the Northern South China Sea Margin Constrained by a Three-dimensional OBS Seismic Velocity Model

Jiazheng Zhang[1*], Minghui Zhao[1,6*], Weiwei Ding[2], César R. Ranero[3,4], Valenti Sallares[3], Jinwei Gao[5], Cuimei Zhang[1], Xuelin Qiu[1,6]

[1]Key Laboratory of Ocean and Marginal Sea Geology, South China Sea Institute of Oceanology, Chinese Academy of Sciences, Guangzhou 510301, China.

[2]Key Laboratory of Submarine Geosciences, State Oceanic Administration, Second Institute of Oceanography, Ministry of Natural Resources, Hangzhou 310012, China.

[3]Barcelona Center for Subsurface Imaging, Instituto de Ciéncies del Mar (ICM-CSIC), Barcelona, Spain.

[4]ICREA, Barcelona, Spain

[5]Laboratory of Marine Geophysics and Deep-Sea Georesource, Institute of Deep-sea Science and Engineering, Chinese Academy of Sciences, Sanya 572000, China.

[6]University of Chinese Academy of Sciences, Beijing 100049, China.

Corresponding author: Jiazheng Zhang (jzzhang@scsio.ac.cn) ; Minghui Zhao (mhzhao@scsio.ac.cn)

Key Points:

- Crustal structure at the northern South China Sea drilled by IODP Expeditions 367/368/368X is unraveled by 3D controlled-source tomography
- Abrupt along-strike change in deformation and magmatism from the NE tectono-magmatic segment to the SW tectonic-dominated segment is found
- Local inherited lithospheric heterogeneities may have caused the along-strike segmentation and the resultant contrasting opening styles

Abstract

A three-dimensional (3D) P-wave seismic velocity (Vp) model of the crust at the northern South China Sea margin drilled by IODP Expeditions 367/368/368X has been obtained with first-arrival travel-time tomography using wide-angle seismic data from a network of 49 OBSs and 11 air-gun shot lines. The 3D Vp distribution constrains the extent, structure and nature of the continental, continent to ocean transition (COT), and oceanic domains. Continental crust laterally ranges in thickness from ~8 to 20 km, a ~20 km-width COT contains no evidence of exhumed mantle, and crust with clear oceanic seismic structure ranges in thickness from ~4.5 to 9 km. A high-velocity (7.0-7.5 km/s) lower crust (HVLC) ranges in thickness from ~1 to 9 km across the continental and COT domains, which is interpreted as a proxy of syn-rift and syn-breakup magma associated to underplating and/or intrusions. Continental crust thinning style is abrupter in the NE segment and gradual in the SW segment. Abrupter continental thinning exhibits thicker HVLC at stretching factor (β) <~3, whereas gentler thinning associates to thinner HVLC at β>~4. Opening of the NE segment thus occurred by comparatively increased magmatism, whereas tectonic extension was more important in the SW segment. The Vp distribution shows the changes in deformation and magmatism are abrupt along the strike of the margin, with the segments possibly bounded by a transfer fault system. No conventional model explains the structure and segmentation of tectonic and magmatic processes. Local inherited lithospheric heterogeneities during rifting may have modulated the contrasting opening styles.

Plain Language Summary

Unravelling the deep structure at the northern South China Sea (SCS) margin drilled by IODP Expedition 367/368/368X can further help understand its rift-to-drift process. A 3D Vp model is therefore constructed with first-arrival travel-time tomography using wide-angle seismic data from a network of 49 OBSs and 11 air-gun shot lines. Based the 3D Vp model, we have identified different kinds of basement domains, including the continental, COT, and oceanic domains. Meanwhile, the HVLC ranging from ~1 to 9 km in thickness across the continental and COT domains is interpreted as a proxy of syn-rift and syn-breakup magmatic underplating and/or intrusions. We find that the continental crust thinning style and magma generation by decompression melting inferred from the HVLC vary along the strike of the margin, demonstrating as NE abrupter thinning with thicker HVLC at stretching factor (β) <~3, whereas

SW gentler thinning with thinner HVLC at β>~4. Hence, our data indicate that a transfer fault system has possibly separated the NE tectono-magmatic segment from the SW tectonic-dominated segment. The segmentation in tectonic and magmatic domains inferred from the 3D Vp model supports that local inherited lithospheric heterogeneities may have led to the different opening styles during rift-to-drift process.

1 Introduction

The continent to ocean transition (COT) is a relevant tectonic unit that develops on the passive continental margin. It is located between the thinned continental crust and the unequivocal oceanic crust, and contains key information about break-up mechanism of continental crust and lithosphere and types of rifted margins (Gao et al., 2015; Peron-Pinvidic et al., 2013; Reston, 2009; Tucholke et al., 2007). Based on the syn-rift and syn-breakup magmatic degree at the COT, the passive continental margins are usually classified into two end members, namely magma-rich and magma-poor margins. The studies of structure and evolution of these margins have attracted a large number of investigations, which have provided a new view on the genesis of the Seaward Dipping Reflector sequences (SDRs) and the high-velocity lower crust (HVLC) on the magma-rich margins (Paton et al., 2017; Holbrook and Kelemen, 1993; White et al., 1987), and on the formation of hyperextended continental crust and/or exhumed serpentinized mantle on the magma-poor margins (Brune et al., 2014; Huismans and Beaumont, 2011; Ranero & Pérez-Gussinyé, 2010; Whitmarsh et al., 2001).

The South China Sea (SCS) is one of the largest marginal seas in the western Pacific (Figure 1). Scientific issues such as its margin nature, evolution process, breakup mechanism are current research topics. Based on previous research results from studies of the COT with ocean bottom seismometer (OBS) and multi-channel seismic (MCS) surveys, the northern SCS was defined either as a magma-poor margin (Wan et al., 2020; Ding et al., 2012; Wang et al., 2006; Yan et al., 2001) or an intermediate rifted margin (Cameselle et al., 2017; Gao et al., 2015; Clift et al., 2001). The International Ocean Discovery Program (IODP) Expeditions 367/368/368X drilled seven sites at the COT of the northern SCS. The rock samples support that the margin experienced a rapid transition from continent to ocean without evidence for mantle exhumations (Childress et al., 2020; Larsen et al., 2018a; Jian et al., 2018; Stock et al., 2018; Sun et al., 2018). This differs from classic magma-poor margins where the continent is juxtaposed with exhumed

serpentinized mantle rocks (Whitmarsh et al., 2001). Therefore, the SCS has been suggested as the "Plate-edge/Pacific" extensional basin, which is different from the Atlantic-type rifted margins (Sun et al., 2019; Wang et al., 2019).

IODP Expeditions 367/368/368X results reveal the presence of a narrow COT (~20 km-width) at the northern SCS (Larsen et al., 2018b), but the processes leading to continental breakup are still debated. Some authors argue that continental breakup was mainly related to a seaward-dipping low-angle extensional fault during latest stage of rifting (Nirrengarten et al., 2020). Similar conclusion is obtained through lateral comparison of the transitional domain structures which show that the continental rupture was mainly controlled by a combination of one or two major listric normal fault(s) rooting near the Moho and a short-duration magmatic event (Ding et al., 2020). However, others propose that the continental breakup is accomplished by core-complex type structures related to a detachment system with flipped polarities (Zhang et al., 2021). Considering the scant information of how structures of rifted continental margins vary along-strike, there are speculations that they could even change within a few tens of kilometers (Peron-Pinvidic et al., 2015; Franke et al., 2014; 2011). However, the new available drilling sites reaching basement and the limited two-dimensional MCS profiles do not provide accurate information on the lateral continuity of the structures and nature of the rocks, and thus there is incomplete understanding on how the thinning of continental crust transitions into oceanic crust formation.

Here, we present and interpret a three-dimensional (3D) P-wave seismic velocity (Vp) model at the northern SCS margin. The model is firstly obtained using controlled-source data acquired at a 3D OBS network that encompasses the seven drilling sites of IODP Expeditions 367/368/368X. Then, we combine the Vp model with the available MCS profiles, free-air gravity anomalies, magnetic lineations and IODP drilling data to interpret the structure, nature and spatial arrangement of the different geological domains. Finally, the structural characteristics and attributes of each domain and their along-strike variations are jointly interpreted to propose a possible geological model for the study area at the northern SCS.

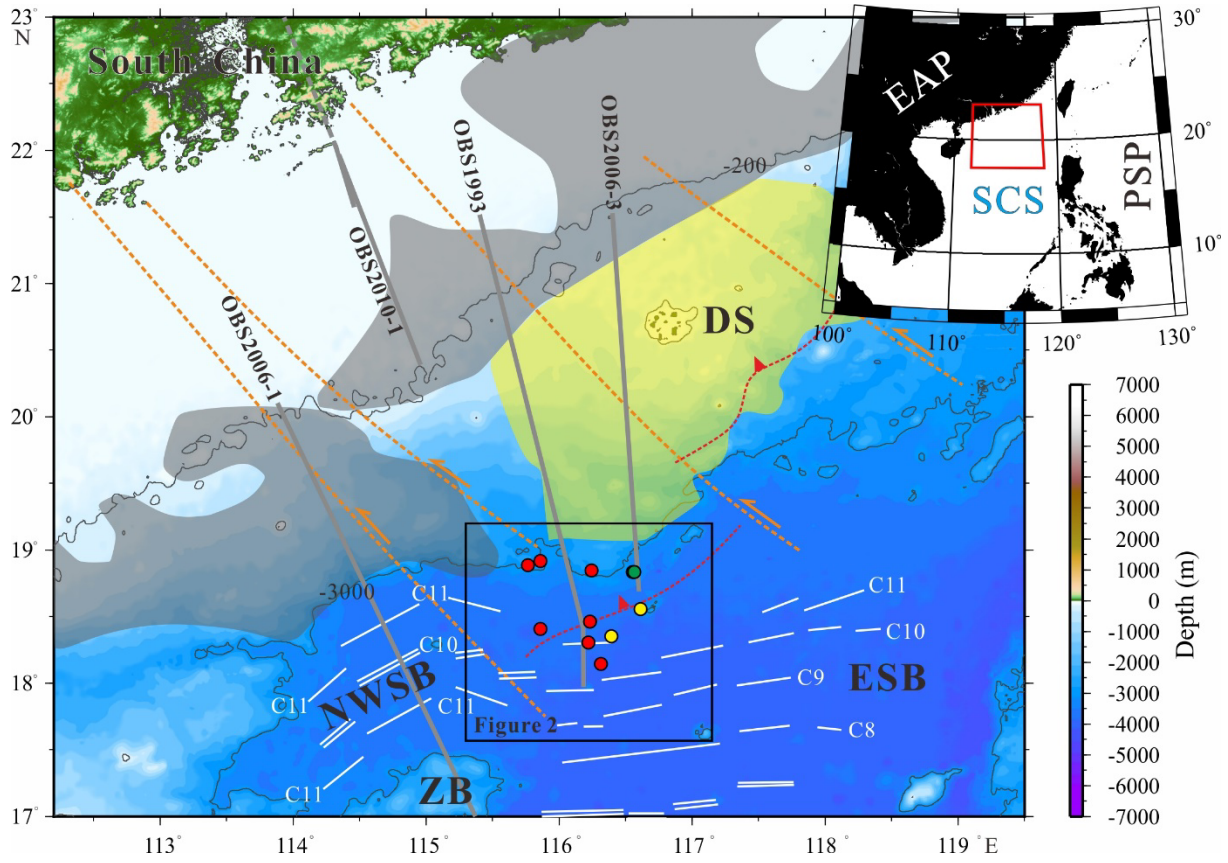

Figure 1. Combined topographic and bathymetric maps of the northern South China Sea (see location map in inset at the right-top corner) showing the distribution of major faults (orange dashed lines) and paleo-Pacific subduction zone (red dashed lines with red triangles) inferred from gravity data (Zhou et al., 2006). The location of the Mesozoic volcanic arc and the Mesozoic forearc basin identified in previous work (Zhao et al., 2019; Li et al., 2018) are shown in gray and yellow shadows, respectively. Seismic lines of OBS1993 (Yan et al., 2001), OBS2006-1 (Ding et al., 2012), OBS2006-3 (Wei et al., 2011) and OBS2010-1 (Cao et al., 2014) are shown in gray. White lines correspond to the magnetic lineations identified by Briais et al. (1993). Drill sites of ODP Leg 184, IODP Expeditions 349, 367/368/368X are indicated by green, yellow and red circles, respectively. Black box shows the location of the study area in Figure 2. SCS: South China Sea; ESB: Eastern Sub-Basin; NWSB: Northwestern Sub-Basin; ZB: Zhongsha Block; DS: Dongsha Island.

2 Geological Setting

The rhomb-shaped boundary of the nowadays SCS was formed under the interaction of the Indo-Australian, Eurasian and Philippine Sea plates. It is widely accepted that, during the Mesozoic, this region where the SCS subsequently developed was a convergent margin with Andean-type volcanic arc and forearc basin, which was affected by different magmatic episodes and was deformed by compressional structures associated with northwestward subduction of the paleo-Pacific plate (Ye et al., 2018; Pubellier & Meresse, 2013; Zhou et al., 2006; Taylor & Hayes, 1983; Holloway, 1981; Figure 1). From the Late Cretaceous to the Early Oligocene, the rollback of the subducted paleo-Pacific plate transformed the paleo-stress field from compression to extension, resulting in multi-stage rifting events, accompanied with local erosion and tectonic uplift (Savva et al., 2014; Li & Li, 2007; Taylor & Hayes, 1983).

In the northern SCS margin, some characteristics of magma-rich and magma-poor margins have been found in previous seismic surveys. For example, HVLC has been observed confined in the northeastern SCS margin (Wang et al., 2006; Yan et al., 2001; Nissen et al., 1995a), although its formation mechanism and age are debated due to the different periods of magmatism on the continental slope (Cheng et al., 2021; Fan et al., 2017; Yan et al., 2006). The hyper-extended continental crust controlled by detachment faults have also been documented in the Pearl River Mouth Basin (Deng et al., 2020; Zhang et al., 2020; Lei et al., 2019; Yang et al., 2018). However, the other important characteristics such as SDRs marked as magma-rich margin and exhumed serpentinized mantle related to magma-poor margin have yet been reported, which make it controversial about the nature of the SCS margin and subsequently confused about its formation mechanism.

Our study area locates at the northern SCS distal margin, where northwestern and northeastern corners seem to connect with the inferred Mesozoic volcanic arc and Mesozoic forearc basin, respectively (Zhao et al., 2019; Li et al., 2018; Figure 1). According to the multibeam bathymetry (Figure 2), the landward part of our study area is separated by a NW-SE extending Pearl River Mouth Canyon which seems to be the surface expression of a Mesozoic major fault (Figure 1) previously inferred by the gravity data (Zhou et al., 2006) and recently confirmed by the MCS profiles (Zhao et al., 2019). A series of basement highs (Figure 2), e.g., outer margin high (OMH) and ridges A/B/C, have been drilled here by the IODP Expeditions 367/368/368X,

but only rocks of continental or oceanic affinities have been found (Childress et al., 2020; Larsen et al., 2018a; Jian et al., 2018; Stock et al., 2018; Sun et al., 2018). Hence, Larsen et al. (2018b) suggest that a rapid transition from continental breakup to igneous oceanic crust occurs in a narrow area of ~20 km-width, which has also been confirmed by subsequent researches (Zhang et al., 2021; Ding et al., 2020).

3 Seismic Experiment and Data Processing

During the Chinese Natural Science Foundation Open Research Cruise of No. NORC2018-08 from May to July 2018, a 3D wide-angle seismic survey was carried out by the R/V Shiyan2 of South China Sea Institute of Oceanology, Chinese Academy of Sciences (CAS) in the northern SCS margin (Figure 2). The seismic source array with a total volume of 6000 in^3 (98.32 L) was composed by four Bolt air-guns towed at a depth of ~10 m. The shooting interval was 90 s at a speed of ~4.5 knots, providing a seismic trace spacing of ~200 m. A total of 8,751 shots were fired along 11 shot lines with a total length of ~1750 km. Fifty-two 4-component short-period (4.5-100 Hz) OBSs made by the Institute of Geology and Geophysics, CAS were deployed with instrument spacing varying from 7 to 10 km, covering a surface of ~30000 km^2. The sampling rates were 4 ms and 10 ms for different instruments. Forty-nine OBSs were finally recovered with effective recording data.

The OBS internal clock drifts were corrected using the time-errors recorded in the logfiles assuming a linear drift during the data collection period. The shot positions were corrected for the offset between the Differential Global Positioning System (DGPS) antenna onboard and the air-guns array. OBSs were relocated by inverting direct water-wave travel-times using a combination of Monte Carlo method and least square method (Yang et al., 2020). The raw data continuously recorded by the OBSs were converted and cut into seismic traces in Society of Exploration Geophysicist (SEGY) format according to the shooting time. The corresponding seismic sections were displayed as reduced time versus offset sections using 3-15 Hz bandpass filtering in order to increase the signal-to-noise ratio (SNR, Figure 3).

This study focuses exclusively on P-wave first arrivals, which are best observed on record sections of the geophone vertical component (Figure 3). The travel time picking steps show as follows: 1) the in-line seismic profile showing the clearest arrivals is picked firstly; 2) the off-line crossing the previous profile is then picked; 3) the rest of seismic sections for each OBS are

finally picked in order. Arrival travel-times were manually picked without differentiating between crustal (e.g., Pg) and mantle phases (e.g., Pn) using the Upicker software (Wilcock, 2011). In total, we finally picked 152,801 first arrival travel-times. The uncertainties for the picked travel-times were calculated based on their SNR within a 200 ms-long window centered by the picked travel-time (e.g., Zelt & Forsyth, 1994).

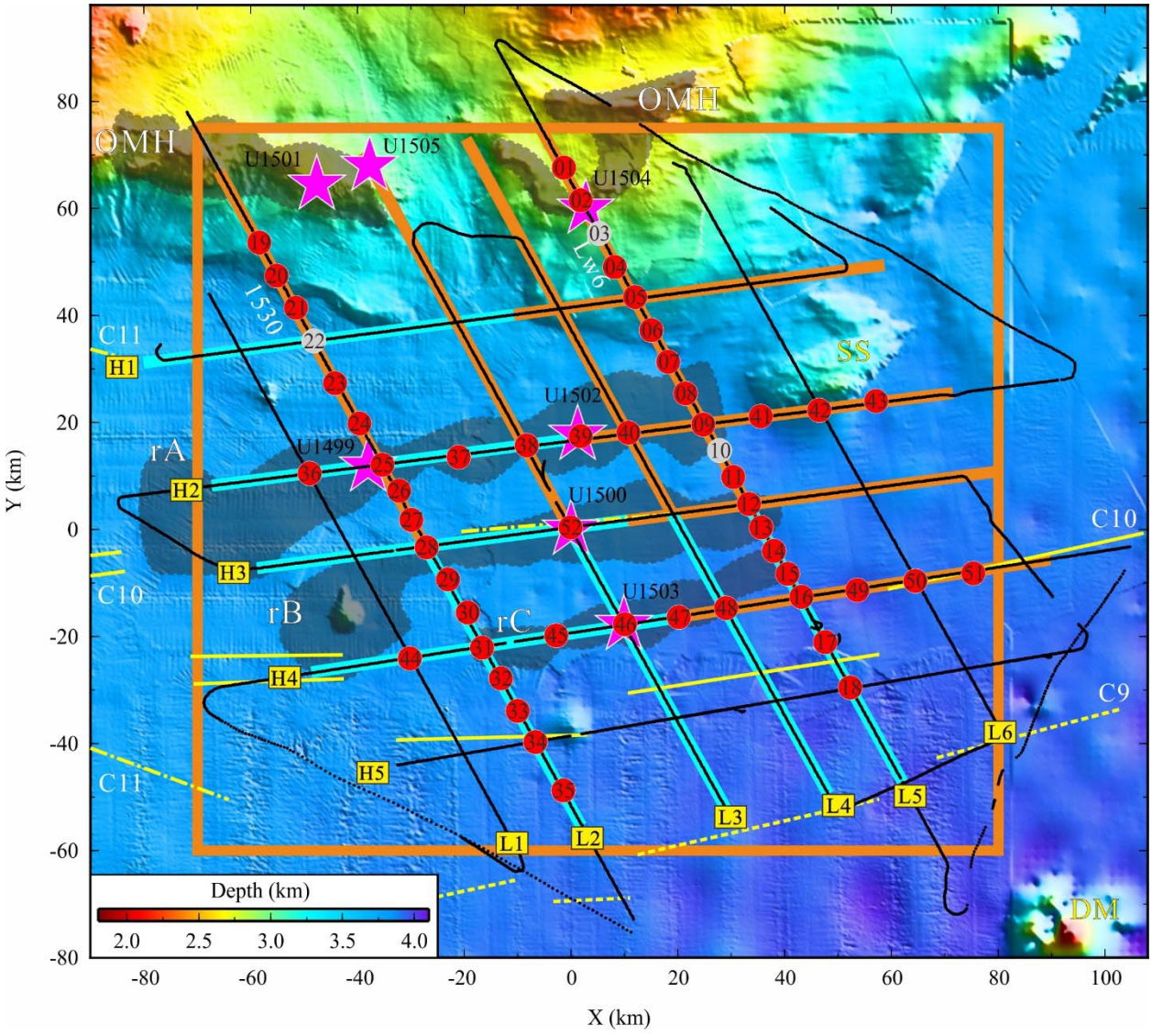

Figure 2. The 3D OBS seismic survey and the multibeam bathymetry map whose original Geographical Coordinate has been transformed into Cartesian Coordinate using shifted Universal Transverse Mercator projection (origin of the local coordinate system corresponds to 116.21992° E, 18.30451° S at OBS52 and site U1500). Red numbered circles display OBSs positions, and black lines with yellow lettered boxes correspond to air-gun shooting tracks. Grey numbered

circles indicate lost OBSs. Yellow dashed-dotted, solid and dashed lines represent magnetic lineations from Briais et al. (1993). Pink stars show drilling sites of IODP Expeditions 367/368/368X. The orange and cyan solid lines show positive and negative parts of the vertical slices of the 3D Vp model shown in Figure 5. The orange box shows the area covered by the horizontal slices shown in Figure 6. The black shaded areas show the basement highs modified from (Larsen et al., 2018b). OMH: outer margin high; rA/rB/rC: basement ridges A/B/C; SS: Shishen Seamount; DM: Daimao Seamount.

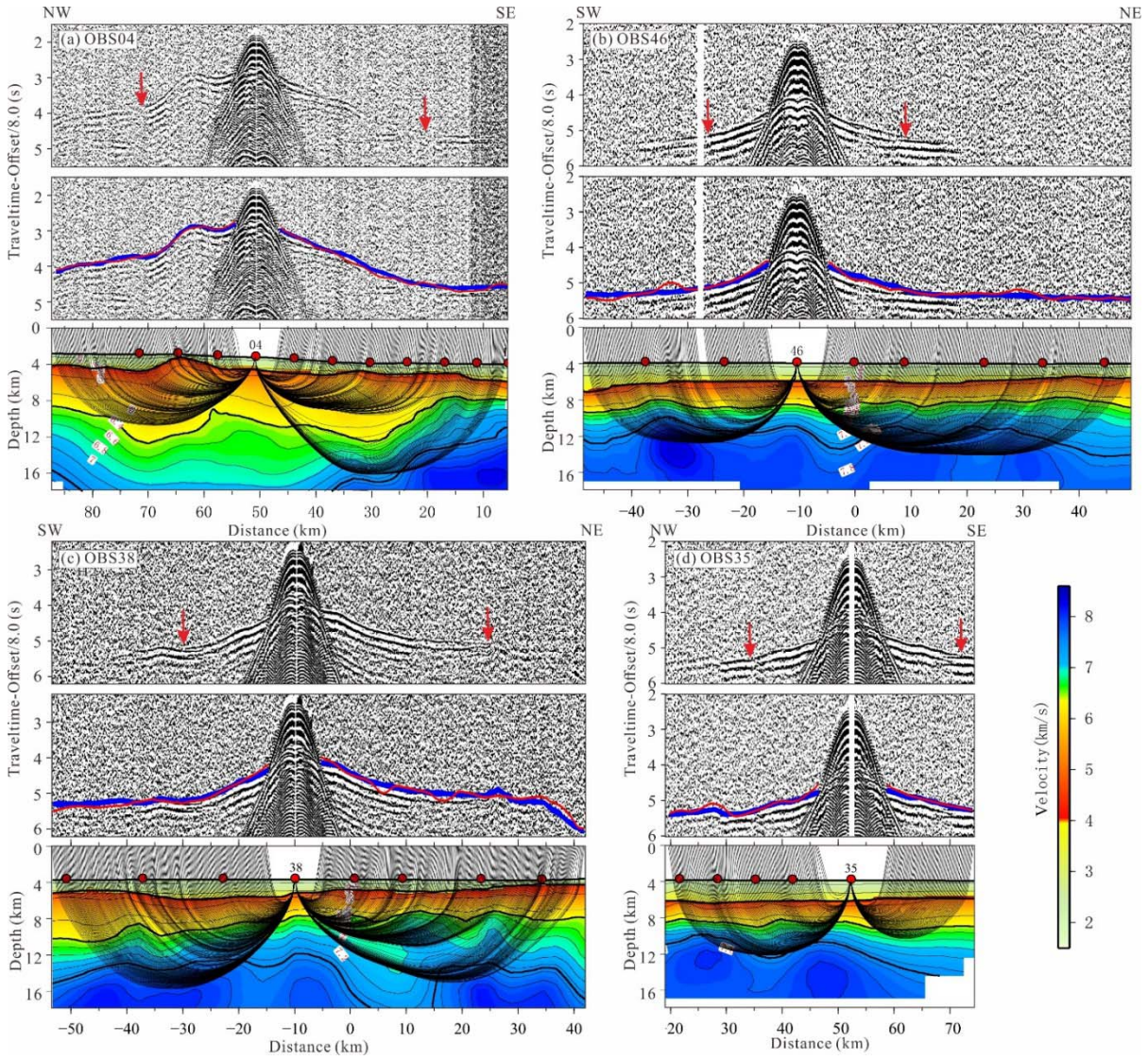

Figure 3. Uninterpreted seismic record sections (upper panel), interpreted seismic sections with blue vertical bars of length equal to the assigned travel-time uncertainty corresponding to observed picks and red lines to the modelled picks (middle panel) and vertical slices of 3D Vp

model with ray-paths (lower panel) along (a) profile L5 for instrument OBS04; (b) profile H2 for OBS46; (c) profile H4 for OBS38; and (d) profile L2 for OBS35. The red circles indicate the locations of OBS. The red arrows show the locations of triple junction of Pg, PmP and Pn.

4 Modeling Method and Results

4.1 Tomography Method

The first arrival seismic tomography code FAST (Zelt & Barton, 1998) is used to build a smooth, isotropic 3D Vp model. FAST solves iteratively a regularized inverse problem to construct a model with the minimum required structure that appropriately fits the observed travel-times. At each iteration, it includes one step of forward modeling (ray tracing) and a second step of travel-time inversion. Forward modeling computes synthetic first arrival travel-times by solving the Eikonal equation based on a finite difference algorithm (Hole & Zelt, 1995; Vidale, 1990). The velocity perturbation is then obtained by minimizing an objective function including norms for the travel-time misfits and model roughness (Shaw & Orcutt, 1985). The velocity perturbation is then added to the initial model and the resulting model is used as a new starting model in the subsequent iterations. This scheme is repeated until the observed travel-times are fit to the level of pick uncertainties (χ^2 close to 1 ideally).

The choice of the starting Vp model is an important step in the setup of any linearized inversion procedure such as the one employed in FAST. In our case, the starting model is composed of three layers such as water, sediment and basement. The layer boundaries corresponding to the seafloor and top of the basement (TOB) are inferred from multibeam bathymetry and from MCS data (Larsen et al., 2018b), respectively. Vp in the water layer is fixed at 1.5 km/s. Vp at the top and bottom of the sedimentary layer are set to 1.5 km/s and 4.0 km/s, varying linearly within this layer. As the study area includes segments of both thinned continental crust and oceanic lithosphere, a one-dimensional (1D) Vp-depth profile roughly falling between the 1D Vp envelop of the thinned continental crust in the northern SCS (Liu et al., 2018) and the 1D Vp of the typical oceanic crust in the Atlantic aged 0-127 Ma (White et al., 1992) is chosen and draped from the TOB to construct the starting 3D Vp model. During iteration, only the velocity structure below the bathymetry is recalculated according to the travel-time misfits.

The regularization parameters of FAST include forward and inverse grid spacing as well as lambda (λ), alpha (α) and iteration times. The λ is a trade-off parameter that controls the relative weighting of fitting the travel time data versus solution constraints. The α controls the relative importance of smoothness/flatness versus smallest perturbation within the regularization part. Based on the 3D modelling experience of the Southwest Indian Ridge (Zhao et al., 2013) and ESB of the SCS (Wang et al., 2016), we conduct a series of tests on the above parameters for a model with dimensions of 198 km×178 km×30 km in X, Y, and Z directions. The spacing of the forward grid is 0.5 km×0.5 km×0.5 km for a total of 8,645,469 nodes, whereas for the inversion grid it is 2 km×2 km×2 km for a total of 132,165 nodes. We have tested different combinations of λ between 0 and 10 and α between 0 and 4. The best fit after five iterations corresponds to a combination of λ=3, and α=0.8. These regularization parameters will also be used in the following tests of uncertainty and resolution of the tomographic Vp models constrained by the same travel-time dataset.

4.2 Uncertainty and Resolution of the Tomographic Model

The solution of any inverse problem depends on the starting model chosen to some extent, and a complete solution must include the measurement of its uncertainty. In order to further assess the influence of the starting model on our final Vp model, a Monte Carlo approach was used to obtain an estimate of the uncertainty (Zhao et al., 2013; Korenaga et al., 2000). One-hundred random 3D starting models were firstly constructed in the same process as described by Section 4.1, in which the 1D Vp-depth profiles were randomly generated in or near the 1D Vp envelops of the thinned continental crust and the typical oceanic crust as mentioned above. Then one-hundred different inversions were executed using the same regularization parameters indicated in Section 4.1.

The average of the RMS misfits from one-hundred inversions is ~107 ms and the corresponding normalized misfit χ^2= ~1.185 (Figure 4). Assuming that the starting models are independent of each other and all solutions are valid (Korenaga et al., 2000), the mean and the standard deviation of the one-hundred solutions will be our final tomographic model (Figures 5&6) and its uncertainty (Figures S1&S2), respectively. The standard deviation has quantified the range of variation (namely uncertainty) in our final Vp models attributed to the different starting models. These values show that the model presents standard deviations <±0.1 km/s in

most of the model, indicating a satisfactory control of seismic velocities. As expected, higher values (>±0.2 km/s) are observed in regions with limited ray coverage (Figures S3&S4), like at the edge or the deeper part of the Vp model (Figures 5&6).

We have also evaluated the resolution of the tomographic model by performing a set of checkerboard tests (Zelt & Barton, 1998). In this way, a total of 55 checkerboard-type models with eleven different squared cell sizes (4, 6, 8, 10, 12, 14, 16, 18, 20, 25 and 50 km), and with a maximum velocity perturbation of 5% have been tested (Figures S5-S8). For each cell size, five different patterns were created with positive and negative polarity without and with spatial shift of 1/4, 2/4, 3/4 and 4/4 of the cell size contemporary at X, Y and Z directions. Each checkerboard pattern was added to the final tomographic model to create each target model and compute the synthetic travel-times. Before inverting each synthetic travel-times dataset, we added a random Gaussian noise, with a standard deviation corresponding to the average picking uncertainty of ~15 ms, to each synthetic travel-time.

After inverting each dataset using the final tomographic model as starting model, we compute the semblance (Figures S9&S10) between the retrieved pattern (Figures S7&S8) and the corresponding target pattern (Figures S5&S6). As in Zelt and Barton (1998), we consider the pattern to be well retrieved for a semblance >0.7. We then compute the average semblance for each cell size and combine them all in a resolution map that depicts the maximum lateral and vertical resolutions of each cell size (Figures S11&S12). All these maps (Figures S11&S12) show that the best resolution areas are located in the central and shallow part of the tomographic model where the minimum cell size that can be retrieved is 4 km. However, the resolution is poor (minimum cell size > 20 km) on the edges and deep part of our model. In these regions the absence of instruments causes a lack of angular coverage because rays cross velocity cells with a common direction, whereas in the deepest part of our model where rays have only horizontal orientation thus decreasing the model resolution.

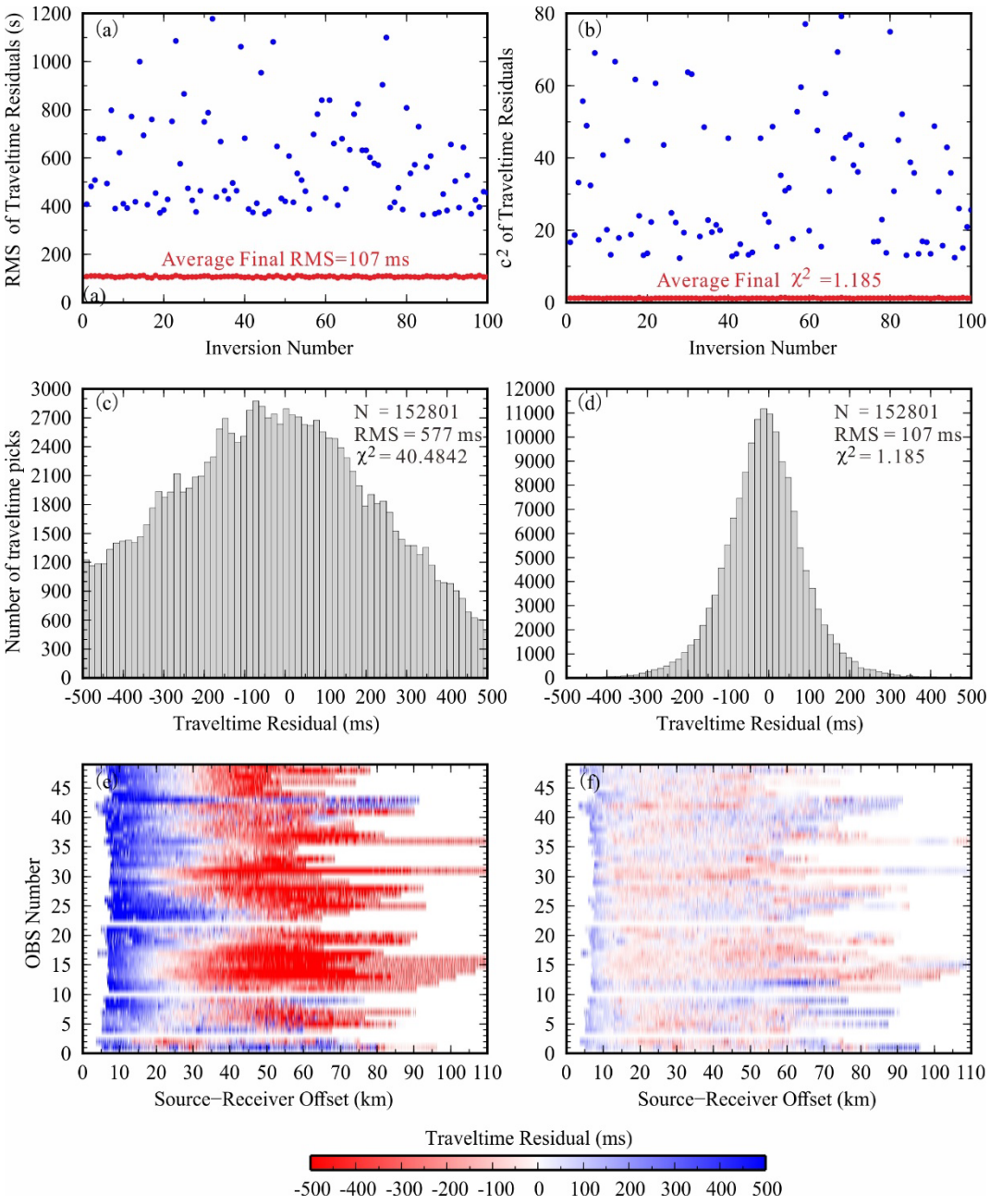

Figure 4. Travel-time residuals distribution for 100 Monte Carlo final solutions. (a) and (b) RMS and χ^2 of travel-time residuals for first (grey dots) and final (red dots) iteration of each Monte Carlo realization, respectively. (c) and (d) Histograms of travel-time residuals for the initial model and the final model, respectively. (e) and (f) Colour-coded travel-time residuals as a function of source-receiver offset (horizontal axis) and OBS number (vertical axis) for the initial model and the final model, respectively.

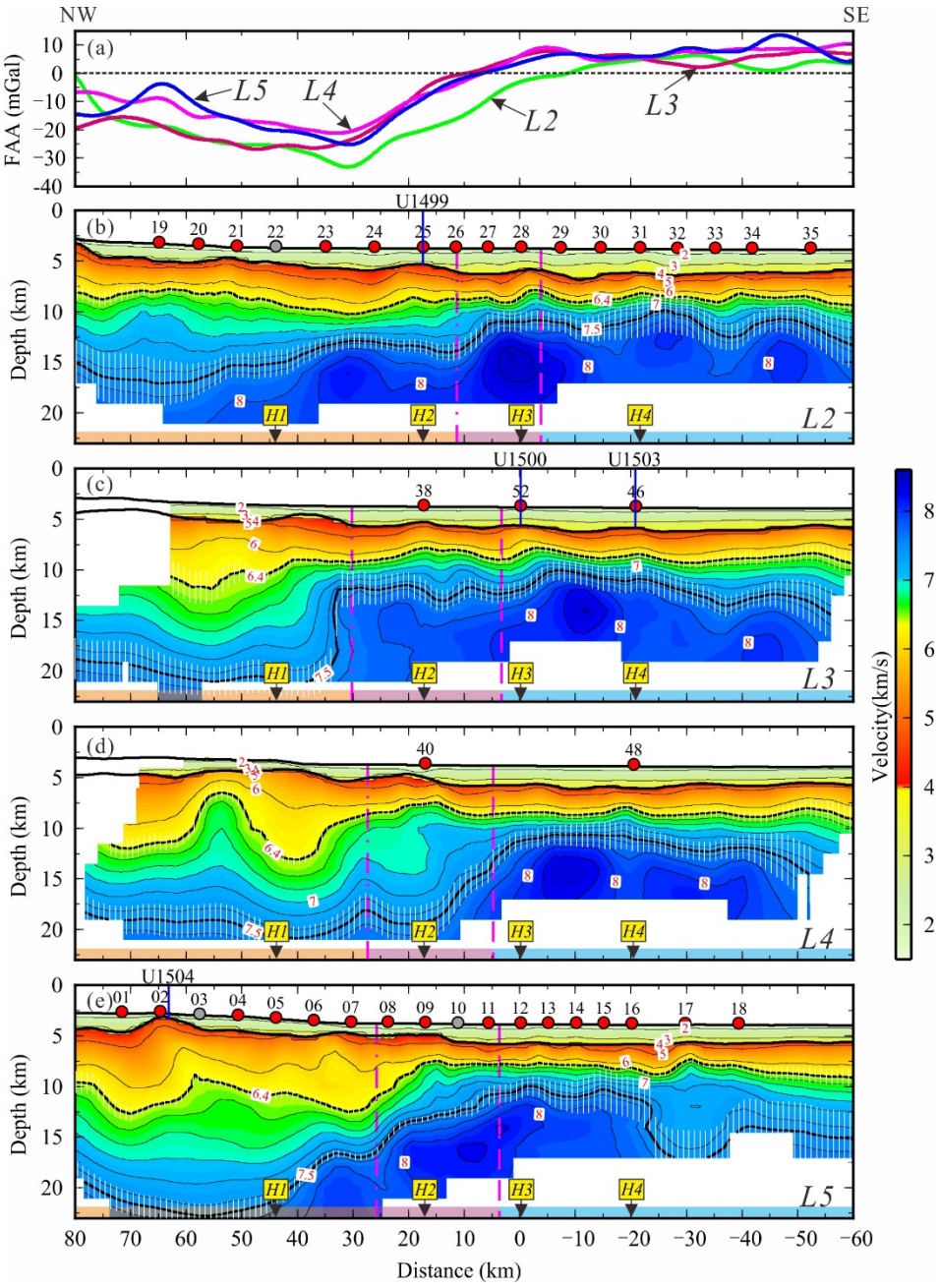

Figure 5. Vertical slices crosscutting the final 3D Vp model and free-air gravity anomaly. (a) Free-air gravity anomalies along shot lines L2, L3, L4 and L5. (b)~(e) Four vertical slices along the extension direction (L2, L3, L4 and L5). (f) Free-air gravity along shot lines H1, H2, H3 and H4. (g)~(j) Four vertical slices along-strike of the margin (H1, H2, H3 and L4). The locations of vertical slices are shown in Figure 2. Masked (white) regions correspond to lack of ray coverage. Velocity contour intervals are 1 km/s in the upper crust and 0.2 km/s in the lower crust, respectively. The 6.4 and 7.5 km/s velocity contours with white vertical bars indicating their

uncertainties are shown as bold contours. Red circles and grey circles are the positions of OBSs used in inversion and lost OBS, respectively. The intersection of two vertical slices are shown by black arrows with letter. The drill sites are shown in blue lines. Pink dashed and dashed-dotted lines mark the seaward and landward boundaries of COT domain, respectively. The yellow, pink and blue horizontal bars represent continental, COT and oceanic domains, respectively.

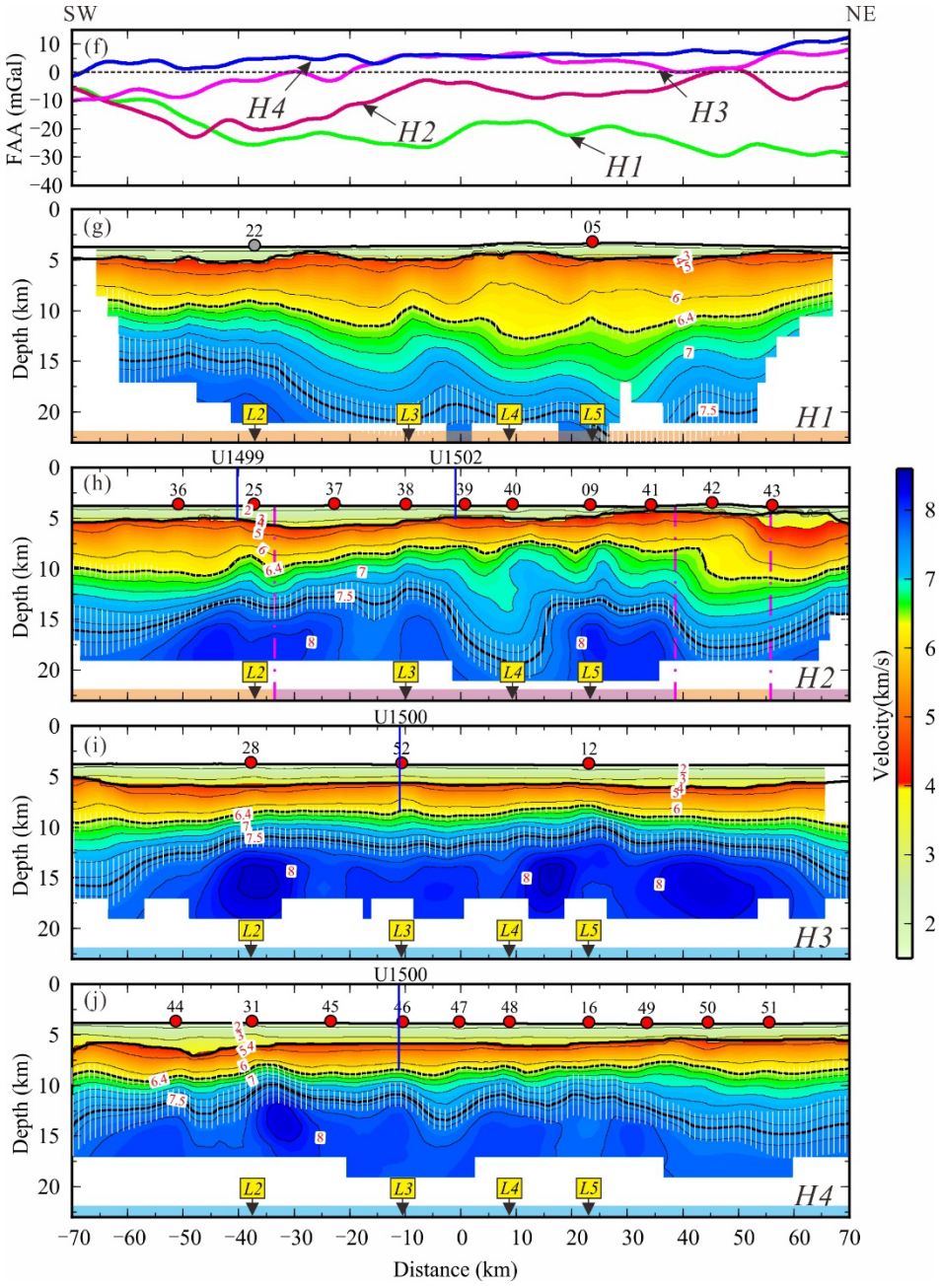

Figure 5 (Continuous).

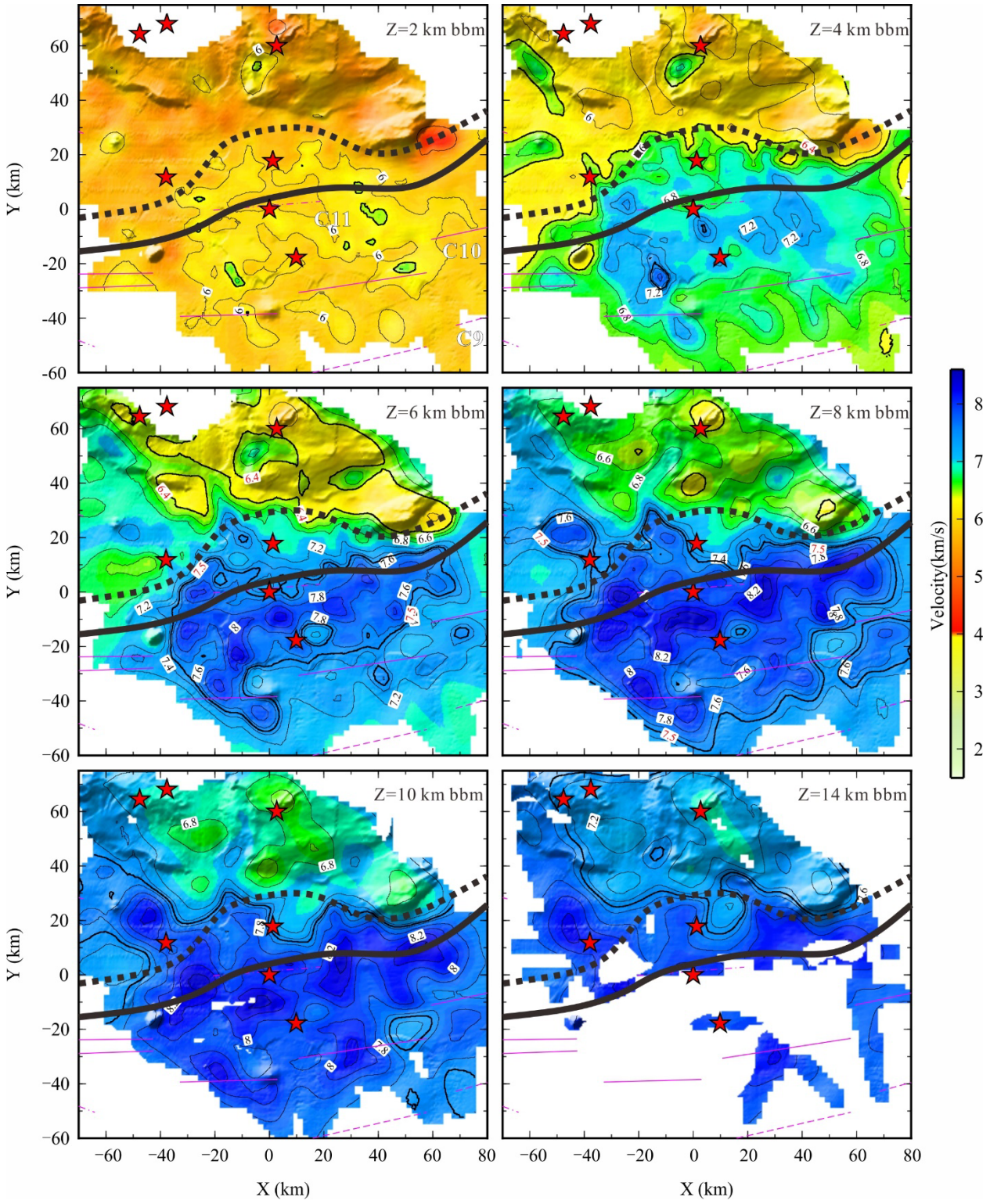

Figure 6. Horizontal slices of the final 3D Vp model at different depths below TOB (bbm). Masked (white) regions correspond to lack of ray coverage. The scope is shown in Figure 2. The 6.4 and 7.5 km/s velocity contours are shown as bold contours. Black solid and dotted lines mark

316 the seaward and landward boundaries of COT domain, respectively. The other symbols are same
317 as the Figure 2.

318 **5 Results**

319 5.1 3D Vp Tomographic Model

320 The final 3D Vp model is our primary result obtained from tomographic inversion (Figures
321 5&6). Vertical slices in this 3D model (Figure 5) correspond to selected dip lines (L2, L3, L4 and
322 L5) and strike lines (H1, H2, H3 and H4) shown in Figure 2. Depth slices are also shown at 2-14
323 km depth below the TOB (bbm), focusing on the central, best resolved part of the model (Figure
324 6). In addition to the Vp model (Figures 5&6), we also show the velocity gradient (Figures
325 S13&S14) and the velocity perturbation models (Figures S15&S16) obtained on each of the
326 slices. The velocity gradient here referred as to vertical velocity variation versus depth is useful
327 to distinguish seismic layers (Zhao et al., 2013; Tong et al., 2003). The velocity perturbation is
328 obtained by subtracting the starting average 1D ensemble from the final model for each node of
329 the 3D Vp model.

330 The velocity, velocity gradient and velocity perturbation models are used to infer the internal
331 layering of the model, although there is no direct inversion of the interfaces in FAST. The 6.4
332 km/s velocity contour, which displays the sharpest variation in the Vp gradient, is inferred to
333 correspond to the boundary between the upper and lower crusts (Figure S13). Two-dimensional
334 (2D) Vp models with reflective interface (Moho) along L2 (Figure S17a&S17b, from Yuan et
335 al., 2022, in submission to Tectonophysics) are obtained using the Rayinvr (Zelt et al., 1992) and
336 TOMO2D (Korenaga et al., 2000), by comparing with which the 7.5 km/s velocity contour in our
337 3D Vp model is taken as the Moho (Figure S17c). As the velocity at the bottom of continental
338 crust is usually less than 7.0 km/s (Christensen & Mooney, 1995), the part of the model above
339 the inferred Moho showing Vp between 7.0 km/s and 7.5 km/s velocity contours is identified as
340 HVLC. The layer between 6.0 and 6.4 km/s velocity contours is tentatively identified as the
341 middle crust which is a potentially key marker for distinguishing the continental and oceanic
342 crusts (Tatsumi, 2008).

343 The vertical slices along L2, L3, L4 and L5 display the 3D Vp model parallel to the extension
344 direction. In general, they have consistent variations in the velocity structures presenting the

seaward uplift of the 7.5 km/s velocity contour (inferred to be a good proxy of the Moho by comparison with the 2D profile) and the resultant tapering of the crustal thickness (Figure 5b-5e). The Moho shallows up from average depths of ~15 km (beneath L2) and ~20 km (beneath L3, L4 and L5) on the landward side to ~11 km on the seaward side, accompanying with reduction of average crustal thickness from ~11-16 km to ~6 km. The seaward variations in crustal structures are also reflected in the free-air gravity anomalies showing gradual transition from negative value to positive value (Figure 5a). Lateral Vp variations indicate similar crustal structure on the seaward side of the 3D model, but great lateral differences on its landward side. In addition to changes in Moho depth, the geometry of 6.4 km/s velocity contour changes from sub-horizontal along L2 to undulating along L3, L4 and L5.

The vertical slices along H1, H2, H3 and H4 run parallel to the margin strike and illustrate that the character of Moho depth and crustal thickness along H1 and H2 changes generally more than those along H3 and H4. Further, there is a greater lateral variation in velocity structure along H1 and H2 than along H3 and H4 (Figure 5g-5j), which is also expressed in change of the free-air gravity anomaly (Figure 5f). Moho depth along H1 diminishes gradually southwestward, from ~20 km (beneath L5) to ~15 km (beneath L2), causing crustal thinning (Figure 5g). Along H2, there is a prominent low velocity anomaly located between L3 and L5, and the nearby site U1502 drilled altered Mid-Ocean Ridge Basalt (MORB) (Figures 5h&S16). The crustal structure along H3 and H4 is similar, with upper and lower crusts ~3 km thick, respectively, although the lower crust is comparatively slightly thicker on the eastern part of H4.

Depth slices further show the Vp lateral variations (Figure 6). The 6.4 km/s velocity occurs as shallow as 2 km bbm in the ocean part, where the Vp and Vp gradient are highest (Figure S14). At 4 km and 6 km bbm, the 6.4 km/s velocity occurs on the entire landward regions, but at 8 km bbm slice it occurs only on the northeastern region. The 7.5 km/s velocity occurs first at 6 km bbm only on the oceanic region, but extends across the entire landward region at 14 km bbm (Figure 6). The variations with depth in distribution of the 6.4 km/s and 7.5 km/s velocities reflect the changes of the upper and lower crust boundary and the Moho resulting from the thinning process (Figure 7a&7b). At 14 km bbm the 7.5 km/s velocity contour near site U1502 seems to form a separated circular structure from the surrounding region displaying a lower velocity anomaly (Figures 6&S16).

375 The distribution of middle crust (6.0-6.4 km/s) is uneven, occurring mainly on the northeastern
376 region with thickness of ~4-6 km, but it is largely absent on the seaward side (thickness < 1 km)
377 (Figure 7c). The HVLC occurs widely, ranging from ~1 to 9 km in thickness (Figure 7d).
378 Although measuring the thickness of HVLC is limited by the difference between the Moho (7.5
379 km/s) in our 3D model and the Moho constrained by PmP (Figure S17), the relative thickness
380 variation is well expressed in the 3D volume. The HVLC on the landward region is generally
381 thicker than that on the seaward region, except near site U1502. Further, the HVLC on the
382 northeastern region is thicker than the southwestern region when comparing along-strike
383 variations (Figure 7d).

384 5.2 Identification of Different Basement Domains

385 The lateral variation in the transition from continental to oceanic crust in 3D defines different
386 basement domains (Figure 8). Previous works with MCS, free-air gravity anomaly (Figure 8),
387 magnetic lineations and recent IODP drilling, proposed basement domains in the study area,
388 including thin continental basement, the COT, and oceanic crust (Zhang et al., 2021; Ding et al.,
389 2020). Based on the variations in whole-crust and middle-crust thickness, as well as 1D Vp-
390 depth profiles from our 3D Vp model, we further investigate the extent, structure and nature of
391 the region. We define the lateral geometry of the COT based on seismic velocity distribution
392 with the seaward boundary to be roughly coincident with the zero value of free-air gravity
393 anomaly corresponding to a ~5-6 km crustal thickness (Figures 7&8), while its landward
394 boundary roughly corresponds to the location where continental crust abruptly thins and the
395 largest crustal thickness variation gradient happens (Figures 5, 7, S17). The landward boundary
396 is also roughly consistent with the maximum negative free-air gravity anomaly, except the parts
397 to the west of L2 and to the east of L5 (Figures 5a, 6&10). Moreover, the landward boundary
398 near drill site U1502 is interpreted landward of a circular-shape crustal thickness anomaly
399 (Figure 7a), because the crustal structure has been modified by magmatism during breakup
400 sampled as altered MORB at site U1502 (Larsen et al., 2018b).

401 The oceanic domain extends across the deep-water region at water depth >~3 km. This domain
402 contains distinct magnetic anomalies, interpreted as seafloor spreading lineations (Li et al., 2014;
403 Briais et al., 1993), positive free-air gravity anomaly (Sandwell et al., 2014), and high-amplitude
404 reflections from TOB displaying a flat to slightly hummocky geometry cut by small-offset faults

and continuous oceanic Moho reflections in seismic images (Zhang et al., 2021; Ding et al., 2020; Ding et al., 2018). Drilling of fresh MORB at sites U1500 and U1503 supports the oceanic nature of this domain (Childress et al., 2020; Larsen et al., 2018a). Our 3D Vp model shows that the average crustal thickness of this region is ~6 km, although it locally ranges from 4.5 to 9 km (Figure 7a). The seismic velocity structure of the basement displays two characteristic layers with a higher velocity gradient in the upper crust and a gentler velocity gradient in the lower crust (Figure 9a) resembling classical oceanic structure (White et al., 1992).

In contrast to the oceanic domain, mainly negative free-air anomalies and no distinct magnetic lineations occur across the continental domain (Li et al., 2014). Syn-rift sediment associated to large-offset faults support a continental rifting style of the basement deformation (Zhang et al., 2021; Ding et al., 2020), confirmed by basement drilling at sites U1501, U1504 and U1505 (Larsen et al., 2018b). Our 3D Vp model displays comparatively thicker basement (~8-20 km) in the continental domain (Figure 7a), whose seismic velocity vertical gradient and perturbation are distinct from those of the oceanic domain (Figures S13-S16). A middle crust layer characterised by 6.0-6.4 km/s velocity and >1 km thick seems to only occur here (Figure 7c). The whole-crust thickness, including upper and middle crust and the HVLC, is thicker in the east sector than in the western sector in this domain. The boundary between these two sectors seems to be consistent with the Pearl River Mouth Canyon shown in the bathymetry (Figure 2). Hence, the continental domain is divided into two segments (Figure 8), which will be discussed in detail in next section. The boundary between the two segments appears to project seaward to a NW-SE elongated area of comparatively thinner basement delineated by the 6 km thickness contour (Figure 7a) across the COT and the oceanic domain, which may be coincident with the Zhongnan fracture zone bounding seafloor spreading segments (Cameselle et al., 2017).

A ~20 km-width COT occurs between the continental and oceanic domains (Figure 8), as the free-air gravity anomaly increases oceanward from negative to positive (Figure 8), which is coincident with the crustal thinning from ~8-14 km on the landside to ~4.5-9 km on the seaside (Figure 7a). The COT basement has been sampled at site U1502 (e.g., altered MORB), supporting the hybrid type of crust based on the sample at comparative site U1499 (e.g., gravels) and the MCS images, where tapering continental crust may have been overprinted by extrusive and underplated/intrusive magmatic material (Zhang et al., 2021; Ding et al., 2020). Gravity modelling using MCS images for structural constraints has interpreted thin continental basement

passing to igneous crust (Nirrengarten et al., 2020). The 1D Vp-depth profiles from the COT domain fall in between typical thin continental and oceanic domains (Figures 9b), which supports hybrid type of crust for the COT basement.

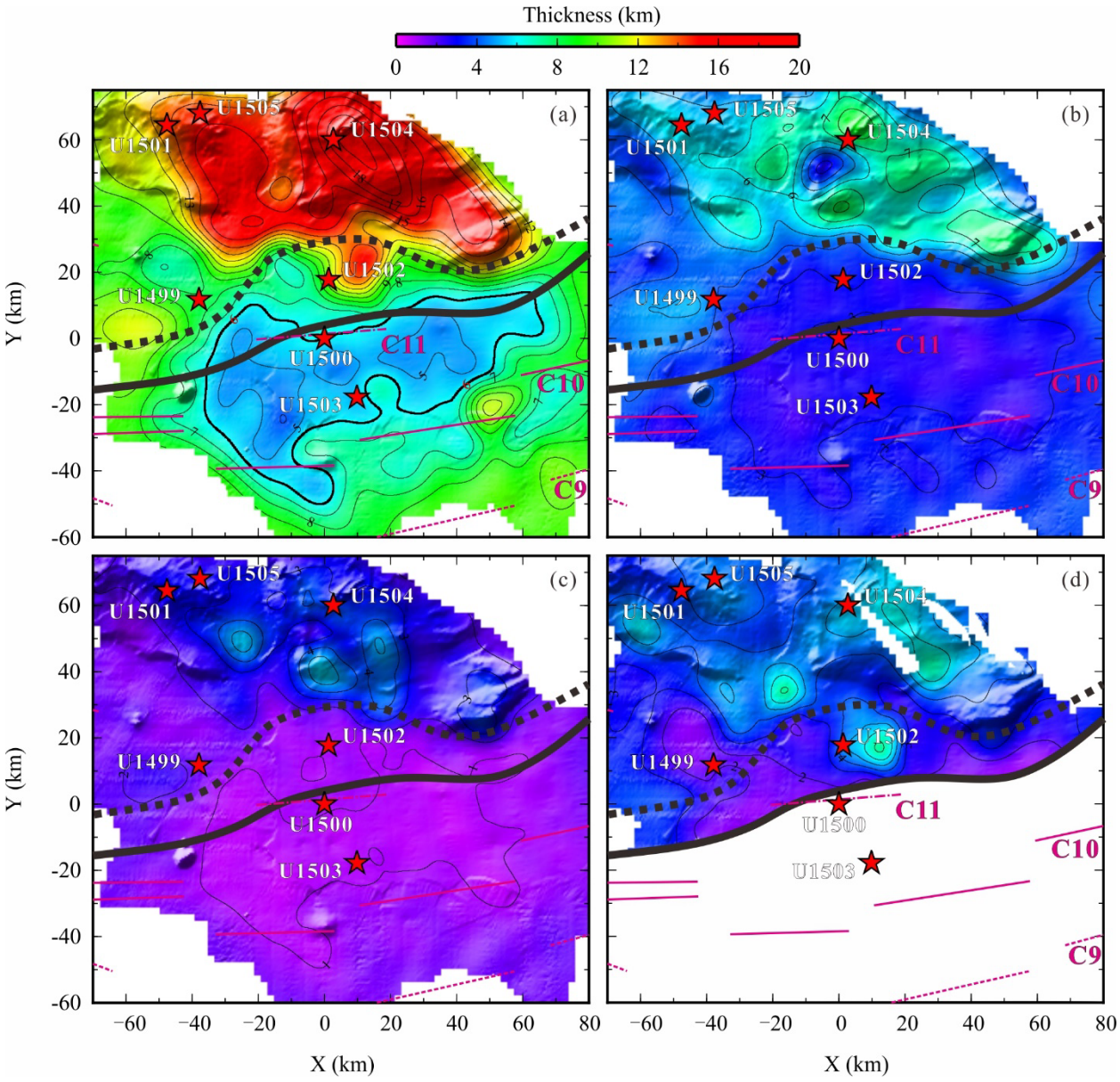

Figure 7. Thickness maps for different layers. (a) Whole crust (between TOB and 7.5 km/s velocity contour). (b) Upper crust (between TOB and 6.4 km/s velocity contour). (c) Middle crust (between 6.0 km/s and 6.4 km/s velocity contours). (d) HVLC (between 7.0 km/s and 7.5 km/s velocity contours). It's worth noting that the layer between 7.0 km/s and 7.5 km/s contours in the oceanic domain is masked as it is usually not referred as to HVLC. The thick black solid

and dotted lines mark the seaward and landward boundaries of COT domain, respectively. The other symbols are same as Figure 2.

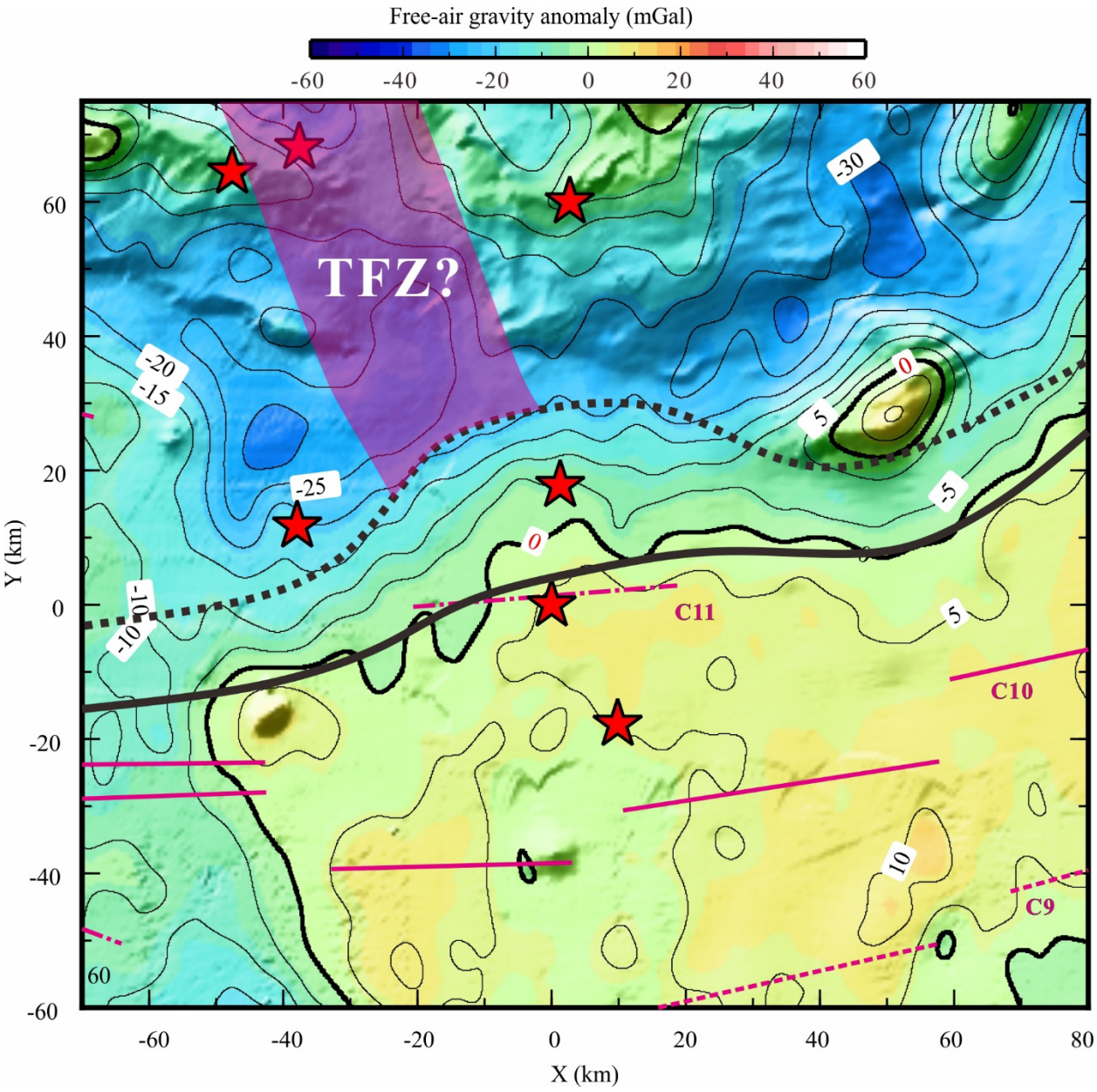

Figure 8. Free-air gravity anomaly map of the study area and identification of different basement domains. The free-air gravity data is from Sandwell et al. (2014). The thick black solid and dotted lines mark the seaward and landward boundaries of COT domain, respectively. The continental and oceanic domains are therefore located on the landward side and on the seaward side, respectively. It is worth noting that a possible transfer fault zone (TFZ) located in the

continental domain has further separated the NE tectono-magmatic segment from SW tectonic-dominated segment. The other symbols are same as Figure 2.

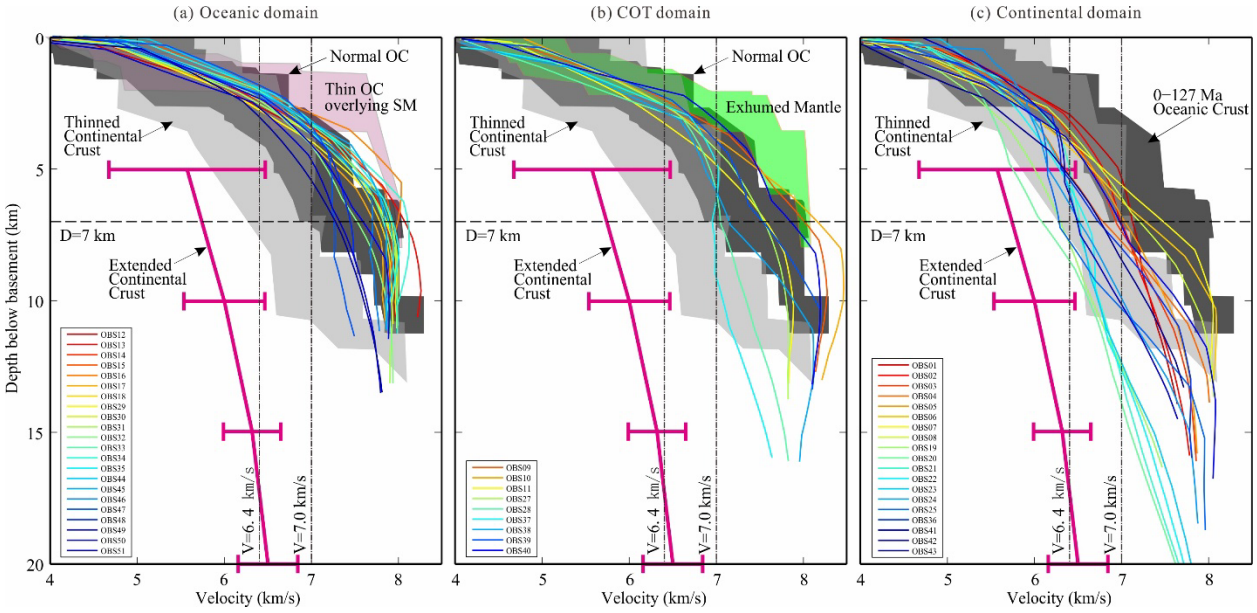

Figure 9. The 1D Vp-depth profiles extracted from the 3D Vp model beneath the OBS stations in (a) the oceanic domain, (b) the COT domain, (c) the continental domain. The dark envelope shows the range of typical velocities for the Atlantic oceanic crust (0-127 Ma) (White et al., 1992). The pink lines with uncertainties indicate extended continental crust (Christensen and Mooney, 1995). The grey envelope indicates the thinned continental crust in the SCS (Liu et al., 2018). The pink envelope and green envelope represent the velocity range of thin oceanic crust overlying serpentinized mantle (Davy et al., 2016; Whitmarsh et al., 1996) and exhumed mantle in the west Iberia margin (Dean et al., 2000).

6 Discussion

6.1 Along-strike crustal changes during end rifting

A major outcome of the 3D Vp model is the along-strike variations in the crustal structure of the continental domain (Figures 5&6). Lateral variations include significant changes in the crust and HVLC thickness (Figure 7). The model shows that there are two styes of thinning along-opening direction from the northeastern (NE) segment to the southwestern (SW) segment, separated by a transfer (fault?) zone marked by an abrupt change in crustal thickness and Vp distribution (Figures 6&7). In the SW segment, continental crust thickness thins towards the

COT from ~13 km to ~8 km in ~70 km range displaying a comparatively gradual thinning, whereas seaward crustal thinning in the NE segment occurs abrupter from ~20 km to ~8 km in ~30 km range (Figure 7a). Both segments transition to oceanic crust across a narrow COT (Figure 8). The two styles of crustal structure are separated by a ~25 km-width NW-SE trending zone (Figure 8). This narrow segment boundary separating two different kinds of tectonic and magmatic styles possibly represents a transfer fault, perhaps relating to the Baiyun-Liwan Fault Zone defined further landward (Zhao et al., 2019).

Contrasting styles of thinning and extension have been described to occur in conjugate margins giving rise to the now classical observation of an asymmetric crustal and tectonic structure (Ranero & Perez-Gussinye, 2010; Hopper et al., 2004). The observed crustal and tectonic asymmetry of conjugate margins led to the term upper-plate margin, in the hanging wall to the inferred lithospheric detachment, and a conjugate lower-plate margin, in the footwall to the detachment (Wernicke, 1995; Lister et al., 1991). Conceptually, upper-plate margin segments might laterally abut a lower-plate margin segment across a transfer fault, causing significant along-strike variation in the crustal structure (Lister, 1986). Along-strike variability from an upper-plate structure to a lower-plate structure have been reported in the SCS (Zhang et al., 2021; Franke et al., 2014; 2011) and for the South Atlantic Angola–Gabon rifted margin (Peron-Pindivic et al., 2015). However, in our study area, there is no MCS images show confident along-strike flip of the detachment polarities (Gao et al., 2015), although it is worth noting that the small-offset faults on the TOB in the NE segment (e.g., Figure 4 in Zhang et al., 2021) are very different from the larger-offset faults (e.g., Figure 13 in Yang et al., 2018) on the TOB in the SW segment, indicating distinct difference in the tectonic deformation between the two segments.

Drilling the northern SCS basement found evidence of syn-rift and syn-breakup magmatism (Sun et al., 2019; Larsen et al., 2018b), and the anomalously high Vp 7.0-7.5 km/s of the HVLC can be interpreted as a proxy of syn-rift and syn-breakup mafic magmatic underplating and lower crustal intrusions. HVLC are often attributed to decompression melting of upwelling hot or chemically anomalous asthenosphere (Sallares et al., 2003; Korenaga et al., 2002). Assuming that most of the HVLC is formed by underplating, it implies crustal stretching factor (β) of ~2-9 when removing the HVLC thickness (Figure S18a&18b) assuming 32 km as initial thickness (Li et al., 2006). It is however somewhat counterintuitive that the HVLC in the NE segment with

smaller β (<~3) is overall thicker than the HVLC in the SW segment with larger β (>~4) (Figures 7d&S18b). Significant differences of the initial lithospheric thickness or mantle potential temperature (Bown & White, 1995; White & McKenzie, 1989) in the relatively small study area appear unlikely (Figure S18c & S18d) and thus the origin of the differences during rifting must come from local chemical or structural heterogeneities.

Potential local lithospheric heterogeneities include inherited lateral changes in mantle composition, which could have modulated the processes that led to the contrasting styles of thinning and magmatism during rifting. Significant changes in magmatism have been reported related to a comparatively strong tectonic segmentation by transform faults in the Gulf of California (Lizarralde et al., 2007). The inheritance of a heterogenous mantle could lead to abrupt along-strike changes in the interplay between deformation and magmatism during end rifting processes. Locally constrained changes in melt production would also influence the lithospheric thermal structure and the crustal and upper mantle rheology so that the opening in the NE segment was controlled by a balance between tectonic and magmatic additions, whereas opening in the SW segment is comparatively dominated by extensional tectonism. This previously unreported relative small-scale segmentation requires a lithospheric scale transfer fault system that separates two different opening styles and two melt generation systems indicated by the distinct HVLC distribution (Figure 10).

6.2 Origin of syn-rift and syn-breakup magmatism

The HVLC in the 3D Vp model may represent sills heavily intruding the lower crust, which may relate to the internal reflection packages in the lower crust above the Moho in MCS images (Ding et al., 2020). The age of the altered MORB drilled at site U1502 (Larsen et al., 2018b) supports the existence of significant syn-rift and syn-breakup magmatism. However, the magmatic budget is inferred moderate compared to magma-rich margins because no SDRs are imaged. The main parameters controlling the onset of magmatic activity and magmatic budget include mantle temperature, opening rate, initial lithospheric thickness (Bown and White, 1995; White and McKenzie, 1989), mantle composition (Sun et al., 2019; Korenaga, 2004) and rifting styles (Lu et al., 2021). Mantle temperature is usually suggested as the main factor to control the formation of the two end-member classes of magma-poor and magma-rich rifted margins (Lu et al., 2021; Minshull et al., 2001; White et al., 1987). Previous investigations speculate on the

presence of a significant positive mantle thermal anomaly during breakup of the northern SCS (Clift et al., 2015; Nissen et al.,1995b), but clearly any existing thermal anomaly was too small to produce structures typical of magma-rich margins.

The Mesozoic paleo-Pacific subduction may have carried abundant fluids into lithosphere prior to the SCS formation (Sun et al., 2019), making its mantle probably different from the north Atlantic rifted margins. An extended phase of rifting occurred in the SCS margins (Cameselle et al., 2020; Franke et al., 2014), and although the main rift event stared in Eocene time and the magmatic event constrained with site U1502 results lasted less than 10 Ma have during which upwelling of asthenosphere generated enhanced magmatism (Ding et al., 2020; Larsen et al., 2018a). However, tectonic extension triggered different magma generation by decompression melting, inferred from the differences in HVLC distribution in the two margin segments (Figure 7d). A possible scenario is that opening rates were significantly different in the two segments and that faster opening of the eastern segment produced larger volume of melt. Alternatively, divergence rates may have been similar along the entire margin sector, but mantle composition differed, and a comparatively more fertile mantle in the eastern segment produced enhanced melt. Although we cannot exclude the first scenario, the second scenario appears more realistic as the NE segment and SW segment may have been located at different tecontic setting in Mesozoic subduction system (Figure 1).

6.3 No mantle exhumation at the COT

Prior to IODP Expeditions 367/368/368X, magma-poor rifting models of the type of the west Iberia margin were often used to interpret the formation of SCS. As a result, the presence of exhumed and serpentinized mantle was interpreted to occur across the COT of the northern SCS, based on interpretations of MCS profiles (Franke et al., 2014). Alternative interpretations of the northern SCS present seismic images displaying continuous Moho reflections from clear continental domains to oceanic domains, and propose a narrow COT containing an abrupt contact between extended continental crust and oceanic igneous crust (Cameselle et al., 2017). A narrow COT between the continental and oceanic domain is supported by drilling results of IODP Expeditions 367/368/368X (Larsen et al., 2018b), that seem to preclude the existence of exhumed mantle in the northern SCS.

562 The drilling results are interpreted to indicate a COT basement made of extended continental
563 crust heavily modified by igneous additions (Zhang et al., 2021; Ding et al., 2020; Nirrengarten
564 et al., 2020). However, the limited number of IODP drilling sites sampling basement at structural
565 highs do not preclude the presence of mantle exhumed by faulting in the drilling area of IODP
566 Expeditions 367/368/368X. For example, because no basement was reached at site U1499, Yang
567 et al (2018) interpret MCS images supporting mantle exhumation. Wan et al (2021) speculate
568 that although fresh MORBs have been drilled at sites U1500 and U1503, a thin igneous carapace
569 may overlie serpentinized exhumed mantle just as interpreted in the west Iberia rifted margin
570 (Davy et al., 2016), or igneous additions occur after exhumation and serpentinization of the
571 mantle as drilled in the Vavilov and Marsili sub-basins of the Tyrrhenian Sea basin (Prada et al.,
572 2020; 2016; 2015).

573 To evaluate the presence of exhumed and serpentinized mantle we compare 1D Vp-depth
574 profiles beneath OBS station across the COT and oceanic domains with those from other basins
575 where exhumed and serpentinized mantle has been confirmed by drilling (Figure 9). The 1D Vp-
576 depth profiles from the oceanic domain fall into the range of velocities for the Atlantic oceanic
577 crust usually referred as normal oceanic crust (White et al., 1992), and do not overlap with the
578 range of velocities of thin magmatic crust overlying serpentinized mantle (Davy et al., 2016;
579 Whitmarsh et al., 1996) (Figure 9a). Furthermore, the 1D Vp-depth profiles from the COT
580 domain fall outside of the range of velocities for the exhumed mantle (Dean et al., 2000), and
581 they fall between the ranges of velocities for thinned continental crust (Liu et al., 2018) and
582 normal oceanic crust (White et al., 1992) (Figure 9b).

583 In addition, distinct and continuous seismic reflection Moho are well displayed in the MCS
584 profiles in or near the study area (Zhang et al., 2021; Ding et al., 2020; Nirrengarten et al., 2020;
585 Cameselle et al., 2017). Furthermore, wide-angle PmP Moho reflections are observed in seismic
586 records at the triple junction of Pg, PmP and Pn (Figure 3). The origin of PmP reflections has
587 been further verified with 2D forward and inverse modeling including the Moho interface
588 (Figure S17). Hence, all available seismic data including the 3D Vp model indicate that mantle
589 exhumation and serpentinization did not occur during the COT formation of the study area.

590 ### 6.4 Rift-to-drift model

591 Different studies (e.g., Cameselle et al., 2020; Deng et al., 2020) propose that the formation
592 and large-scale evolution of the SCS is similar to the "wide rift mode" of extension (Hopper &
593 Buck, 1996; Buck, 1991). A ~1000 km-wide region of continental crust formed by “basin and
594 ranges” with a crustal architecture characterized by a succession of thin-basement (<~10 km)
595 sub-basins (e.g., the Xisha failed rift and Baiyun-Liwan Sags) separated by basement highs
596 (Cameselle et al., 2020; Clerc et al., 2018; Franke et al., 2014; Savva et al., 2014). These sub-
597 basins possibly evolved as discrete subsystems during early rifting, with final breakup and the
598 transition to seafloor spreading only occurred in one of them (Cameselle et al., 2020). The 3D
599 Vp model provides unprecedented resolution of the lateral crustal variability to study the end
600 phase of rifting and how the deformation localized in 3D (Figure 10).

601 Early stretching deformation is decoupled between the ductile lower crust and the brittle upper
602 crust, with a series of discrete small-scale normal faults cutting TOB (Franke et al., 2014). These
603 comparatively small faults are observed onshore (Nanni et al., 2017) and extend offshore. When
604 the crust is thinned to <~15 km, differences in rheology and the result of the interplay between
605 magmatism and faulting become more evident. In area with a ductile lower crust and limited
606 magmatism, basin-bounding faults develop as detachment surfaces giving rise to fault-controlled
607 thinning like in the Liwan sag with long detachment fault (>100 km) that extends towards the
608 COT characterized by numerous tilted blocks (e.g., along L2, Yang et al., 2018). Thinning
609 towards the COT in the SW segment is gradual as the motion between upper and lower
610 crust/upper mantle is accommodated along the detachment surfaces (Figure 10).

611 In contrast, tectonic deformation is comparatively less intense in the NE segment,
612 accompanied by thicker middle crust and the magmatic production associated to the HVLC
613 (Figure 7c&7d). Local lithospheric heterogeneities may have caused more magma in the NE
614 segment than that in the SW segment and the accommodation space created during the basin
615 opening is filled by a comparatively larger proportion of magmatic intrusions and relatively
616 smaller-offset normal faulting restricted to the upper crust (Figure 10).

617 Deeply penetrating faults are usually inferred to promote the exhumation and eventual
618 exposure at the seafloor of originally deep-seated material, either lower crust or mantle (Reston,
619 2009; Manatschal et al., 2001). However, neither mantle or lower crust exhumation are a

requisite in the SCS rifting. The northern SCS magmatism may not only have contributed to form the HVLC, but also potentially used fault systems of the COT to percolate through highly-thinned continental crust, forming the hybrid COT domain of thin continental crust and igneous additions (Figure 10). Final breakup likely occurred rapidly associated to the weakening produced by magmatic diking as lithospheric thinning progressed.

The north Atlantic rifted margins have been the most widely studied. Scientists have carried out extensive geological and geophysical surveys to reveal the crustal structure (Minshull et al., 2009), as well as numerous numerical and physical modelling to study what parameters have influenced the rifting styles. A large number of geodynamic and conceptual models have been proposed (Brune et al., 2014; Huisman & Beaumont, 2011; Ranero & Perez-Guissinye, 2010; Whitmarsh et al., 2001), and have been widely applied to other rifted margins. However, the new 3D Vp data provides information on the rift-to-drift transition process for the northern SCS that is different from the classic magma-poor and magma-rich rifted margins. In the future, the 3D physical and numerical modelling are proposed to verify and reveal what kinds of parameters mainly control the rifting style which may be very different from that in the Atlantic rifted margins.

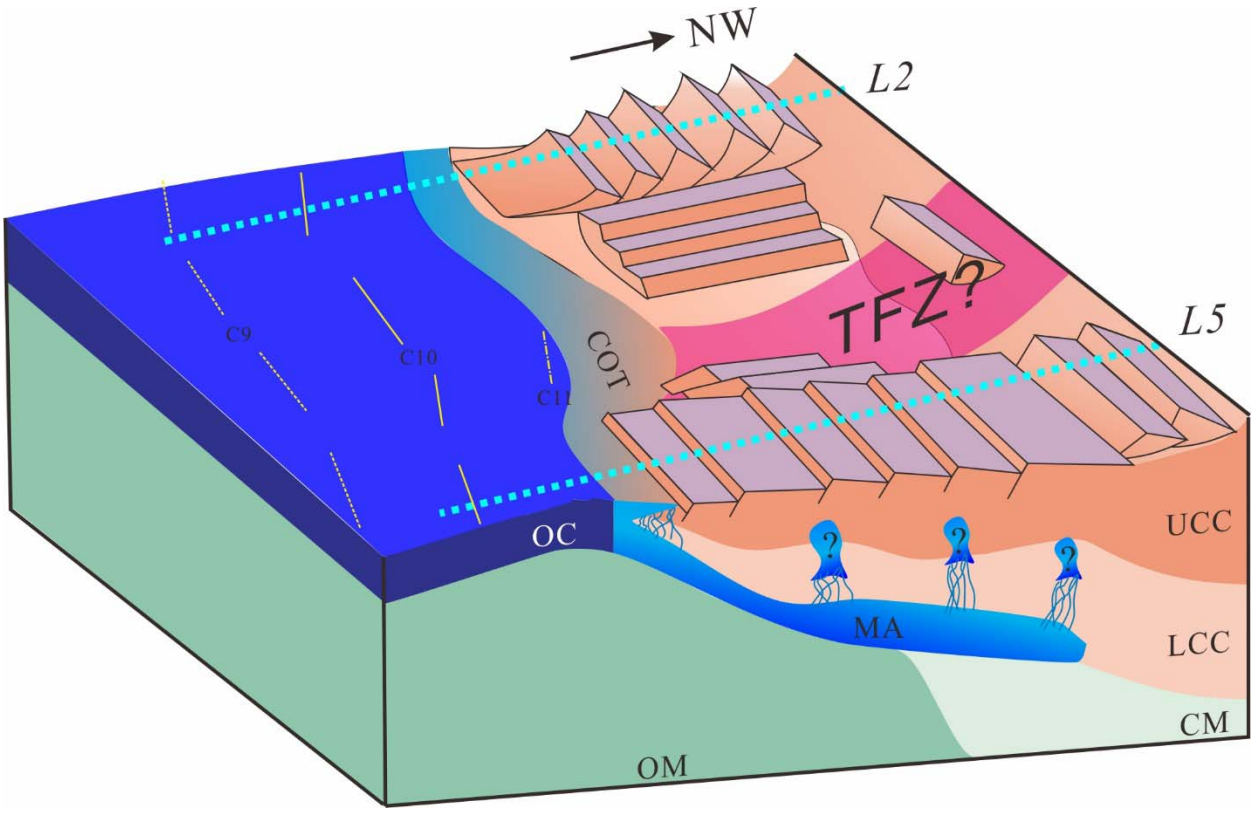

Figure 10. Schematic diagram showing possible geological model with possible tectonics and magmatism during rift-to-drift process in the study area. An abrupt along-strike change in deformation and magmatism occurred from the NE segment to SW segment. Magmatism in the NE segment was abundant and took a significant proportion of the opening leading to a comparatively smaller scale faulting of the upper crust. Whereas the SW segment was dominated by tectonic extension and magmatism played a comparatively minor role during opening. The two contrasting segments were bounded possibly by a transfer fault system that provided the differential slip during opening of the two different crustal thinning styles and the magmatism leading to the different HVLC distribution. The crustal structure along L2 and L5 in cyan lines are shown in Figure 5. UCC: Upper continental crust; LCC: Lower continental crust; OC: Oceanic crust; MA: Magmatic addition; CM: Continental mantle; OM: Oceanic mantle; TFZ: Transfer fault zone.

7 Conclusions

In order to further reveal the rift-to-drift process in the northern SCS distal margin, a 3D OBS Vp model is obtained using the first-arrival travel-time tomography method. In combination with the geological and geophysical data, we have some new insights as following.

1) The 3D Vp distribution determines the extent of the continental, COT and oceanic domains. The continental domain displays significant lateral variations in thickness from the maximum of ~20 km at the NE segment to the minimum of ~8 km at the SW segment. The oceanic domain shows crustal thickness of ~4.5-9 km with an average of ~6 km, with clear oceanic type seismic structure. A narrow COT domain with width of ~20 km occurs between the continental and oceanic domains.

2) The NE abrupt thinning and SW gradual thinning of crustal thickness are observed along-strike margin. Meanwhile, the HVLC interpreted as a proxy of syn-rift and syn-breakup magma shows thicker at the NE region of continental domain with smaller β ($<\sim3$) than that at the SW region with larger β ($>\sim4$). We suggest that this indicates the juxtaposition of NE tectono-magmatic segment and SW tectonic-dominated segment, which is bounded possibly by a transfer fault system.

665 3) The rapid extension during late Eocene may be responsible for the rapid upwelling of the
666 asthenosphere and moderate magma produced by decompression melting. However, the local
667 lithospheric heterogeneities due to Mesozoic paleo-Pacific subduction have caused different
668 magmatic production along the strike of the margin. This magmatic event not only forms the
669 HVLC, but also alters the highly-thin continental crust to form a narrow COT domain with
670 hybrid crust.

671 4) The segmentation in rifting style observed at the northern SCS is unprecedented and can
672 not easily be explained by current models of rifting. The contrast in extension styles and inferred
673 magmatism, separated by distinct transfer zone may imply that inherited mantle heterogeneities
674 played a major role during rifting. High resolution seismic Vp models are needed to test the
675 significant of segmentation in other rift systems.

676 **Acknowledgments**

677 Discussions with Enyuan He, Haibo Huang, Yuhan Li and Zhongxian Zhao are constructive to
678 better understanding the rift-to-drift process in general. This work is financially supported by
679 National Natural Science Foundation of China (Grant Nos. 41730532, 91958212, U20A20100).
680 We thank the crew and scientists of the R/V Shiyan 2 of South China Sea Institute of
681 Oceanology, CAS for their contributions during the data acquisition of Chinese Natural Science
682 Foundation Open Research Cruise (Cruise No. NORC2018-08). Some figures were produced by
683 Generic Mapping Tools (GMT) software (Wessel et al., 2013).

684 **Open Research**

685 The raw data used for P-wave travel-time tomographic inversion in this study is available at
686 Science Data Bank via https://www.scidb.cn/anonymous/ckVyTVpm with CC0 (Zhang J., Zhao,
687 M., & Qiu X., 2022).

688 **References**

689 Bown, J. W., & White, R. S. (1995). Effect of finite extension rate on melt generation at rifted
690 continental margins. *Journal of Geophysical Research: Solid Earth, 100(B9)*, 18011-
691 18029, https://doi.org/10.1029/94JB01478
692 Briais, A., Patriat, P., & Tapponnier, P. (1993). Updated interpretation of magnetic anomalies
693 and seafloor spreading stages in the south China Sea: Implications for the Tertiary tectonics

694 of Southeast Asia. *Journal of Geophysical Research: Solid Earth, 98(B4)*, 6299-6328.
695 https://doi.org/10.1029/92JB02280
696 Brune, S., Heine, C., Pérez-Gussinyé, M, & Sobolev, S. V. (2014). Rift migration explains
697 continental margin asymmetry and crustal hyper-extension. *Nature Communications, 5*.
698 https://doi.org/10.1038/ncomms5014
699 Buck, W. R. (1991). Modes of continental lithospheric extension. *Journal of Geophysical*
700 *Research: Solid Earth, 96(B12)*, 20161-20178. https://doi.org/10.1029/91JB01485
701 Cameselle, A. L., Ranero, C. R., & Barckhausen, U. (2020). Understanding the 3D formation of
702 a wide rift: the central South China Sea rift system. *Tectonics, 39(12)*,
703 e2019TC006040. https://doi.org/10.1029/2019TC006040
704 Cameselle, A. L., Ranero, C. R., Franke, D., & Barckhausen, U. (2017). The continent-ocean
705 transition on the northwestern South China Sea. *Basin Research, 29*, 73-95.
706 https://doi.org/10.1111/bre.12137
707 Cao, J., Sun, J., Xu, H., & Xia, S. (2014). Seismological features of the littoral fault zone in the
708 Pearl River Estuary. *Chinese Journal of Geophysics (in Chinese), 2014, 57(2)*, 498-508.
709 https://doi.org/10.6038/cjg20140215
710 Cheng, J., Zhang, J., Zhao, M., Du, F., Fan, C., & Wang, X., et al. (2021). Spatial distribution
711 and origin of the high-velocity lower crust in the northeastern South China Sea.
712 *Tectonophysics, 819*, 229086. https://doi.org/10.1016/j.tecto.2021.229086
713 Childress, L.B., Alvarez Zarikian, C.A., Briais, A., Dadd, K.A., Deng, J.-M., & Höfig, T.W., et
714 al. (2020). Expedition 368X Preliminary Report: South China Sea Rifted
715 Margin. *International Ocean Discovery Program*.
716 https://doi.org/10.14379/iodp.proc.368X.101.2020
717 Christensen, N. I., & Mooney, W. D. (1995). Seismic velocity structure and composition of the
718 continental crust: A global view. *Journal of Geophysical Research Atmospheres, 100(B6)*,
719 9761-9788. https://doi.org/10.1029/95JB00259
720 Clerc, C., Ringenbach, J. C., Jolivet, L., & Ballard, J. F. (2018). Rifted margins: ductile
721 deformation, boudinage, continentward-dipping normal faults and the role of the weak
722 lower crust. Gondwana Research, 53, 20-40. https://doi.org/10.1016/j.gr.2017.04.030

723 Clift, P. D., & Lin, J. (2001). Patterns of extension and magmatism along the continent-ocean
724 boundary, south china margin. *Geological Society London Special Publications, 187(1)*,
725 489-510. https://doi.org/10.1144/GSL.SP.2001.187.01.24
726 Clift, P. D., Brune, S., & Quinteros, J. (2015). Climate changes control offshore crustal structure
727 at South China Sea continental margin. *Earth and Planetary Science Letters, 420*, 66-72.
728 https://doi.org/10.1016/j.epsl.2015.03.032
729 Davy, R. G., Minshull, T. A., Bayrakci, G., Bull, J. M., Klaeschen, D., & Papenberg, C., et
730 al. (2016), Continental hyperextension, mantle exhumation, and thin oceanic crust at the
731 continent-ocean transition, West Iberia: New insights from wide-angle seismic. *Journal of*
732 *Geophysical Research: Solid Earth, 121(5)*, 3177-3199.
733 https://doi.org/10.1002/2016JB012825
734 Dean, S. M., Minshull, T. A., Whitmarsh, R. B., & Louden, K. E. (2000). Deep structure of the
735 ocean-continent transition in the southern Iberia Abyssal Plain from seismic refraction
736 profiles: the IAM-9 transect at 40°20′N. *Journal of Geophysical Research: Solid Earth,*
737 *105(B3)*, 5859-5886. https://doi.org/10.1029/1999JB900301
738 Deng, H., Ren, J., Pang, X., Rey, P. F., & Luo, P., et al. (2020). South China Sea documents the
739 transition from wide continental rift to continental break up. *Nature Communications, 11(1)*,
740 4583. https://doi.org/10.1038/s41467-020-18448-y
741 Ding W., Sun Z., Mohn G., Nirrengarten M., Tugend J., & Manatschal G., et al. (2020). Lateral
742 evolution of the rift-to-drift transition in the South China Sea: Evidence from multi-channel
743 seismic data and IODP Expeditions 367&368 drilling results. *Earth and Planetary Science*
744 *Letters, 531*, 115932. https://doi.org/10.1016/j.epsl.2019.115932
745 Ding, W., Schnabel, M., Franke, D., Ruan A., & Wu, Z. (2012). Crustal structure across the
746 northwestern margin of South China Sea: evidence for magma-poor rifting from a wide-
747 angle seismic profile. *Acta Geologica Sinica-English Edition*, *86(4)*, 854-866.
748 https://doi.org/10.1111/j.1755-6724.2012.00711.x
749 Ding, W., Zhen, S., Dadd, K., Fang, Y., & Li, J. (2018). Structures within the oceanic crust of
750 the central south china sea basin and their implications for oceanic accretionary processes.
751 *Earth and Planetary Science Letters, 488*, 115-125.
752 https://doi.org/10.1016/j.epsl.2018.02.011

753 Fan, C., Xia, S., Zhao, F., Sun, J., Cao, J., & Xu, H., et al. (2017). New insights into the
754 magmatism in the northern margin of the South China Sea: spatial features and volume of
755 intraplate seamounts. *Geochemistry Geophysics Geosystems, 18(6)*, 2216-2239.
756 https://doi.org/10.1002/2016GC006792
757 Franke, D., Barckhausen, U., Baristeas, N., Engels, M., Ladage, S., & Lutz, R., et al. (2011). The
758 continent-ocean transition at the southeastern margin of the South China Sea. *Marine and*
759 *Petroleum Geology, 28(6)*, 1187-1204. https://doi.org/10.1016/j.marpetgeo.2011.01.004
760 Franke, D., Savva, D., Pubellier, M., Steuer, S., Mouly, B., & Auxietre, J. L., et al. (2014). The
761 final rifting evolution in the South China Sea. *Marine and Petroleum Geology, 58*, 704-720.
762 https://doi.org/10.1016/j.marpetgeo.2013.11.020
763 Gao, J., Wu, S., McIntosh, K., Mi, L., Yao, B., & Chen, Z., et al. (2015). The continent–ocean
764 transition at the mid-northern margin of the south china sea. *Tectonophysics, 654*, 1-19
765 https://doi.org/10.1016/j.tecto.2015.03.003
766 Holbrook, W. S., & Kelemen, P. B. (1993). Large igneous province on the us atlantic margin and
767 implications for magmatism during continental breakup. *Nature, 364(6436)*, 433-436.
768 https://doi.org/10.1038/364433a0
769 Hole, J. A., & Zelt, B. C. (1995). Three-dimensional finite-difference reflection travel-times.
770 *Geophysical Journal International, 121(2)*, 427-434. https://doi.org/10.1111/j.1365-
771 246X.1995.tb05723.x
772 Holloway, N. H. (1981). The north Palawan block, Philippines: its relation to the Asian mainland
773 and its role in the evolution of the South China Sea. *Geological Society of Malaysia*
774 *Bulletin, 14*, 19-58. https://doi.org/10.7186/bgsm14198102
775 Hopper, J. R., Funck, T., Tucholke, B. E., Larsen, H. C., Holbrook, W. S., & Louden, K. E., et
776 al. (2004). Continental breakup and the onset of ultraslow seafloor spreading off Flemish
777 cap on the Newfoundland rifted margin. *Geology, 32(1), 93-96*.
778 https://doi.org/10.1130/G19694.1
779 Hopper, J. R., & Buck, W. R. (1996). The effect of lower crustal flow on continental extension
780 and passive margin formation. *Journal of Geophysical Research: Solid Earth, 101(B9)*,
781 20175-20194. https://doi.org/10.1029/96JB01644

782 Huismans, R., & Beaumont, C. (2011). Depth-dependent extension, two-stage breakup and
783 cratonic underplating at rifted margins. *Nature, 473(7345)*, 74-78.
784 https://doi.org/10.1038/nature09988
785 Huismans, R., & Beaumont, C. (2011). Depth-dependent extension, two-stage breakup and
786 cratonic underplating at rifted margins. *Nature, 473(7345)*, 74-78.
787 https://doi.org/10.1038/nature09988
788 Jian, Z., Larsen, H.C., Alvarez Zarikian, C.A., Sun, Z., Stock, J.M., Klaus, A., et al. (2018). Site
789 U1505. *In: Proceedings of the International Ocean Discovery Program, 367/368*.
790 https://doi.org/10.14379/iodp.proc.367368.109.2018
791 Korenaga, J., Holbrook, W. S., Kent, G. M., Kelemen, P. B., Detrick, R. S., & Larsen, H. C., et
792 al. (2000). Crustal structure of the southeast Greenland margin from joint refraction and
793 reflection seismic tomography. *Journal of Geophysical Research: Solid Earth, 105(B9)*,
794 21591-21614. https://doi.org/10.1029/2000JB900188
795 Korenaga, J., Kelemen P.B., & Holbrook W. S. (2002) Methods for resolving the origin of large
796 igneous provinces from crustal seismology. *Journal of Geophysical Research: Solid Earth,*
797 *107(B9)*, 1-27. https://doi.org/10.1029/2001JB001030
798 Korenaga J. (2004). Mantle mixing and continental breakup magmatism. *Earth and Planetary*
799 *Science Letters, 218(3-4)*, 463-473. https://doi.org/10.1016/S0012-821X(03)00674-5
800 Larsen, H.C., Sun, Z., Stock, J.M., Jian, Z., Alvarez Zarikian, C.A., & Klaus, A., et al. (2018a).
801 Expedition 367/368 summary. *In: Proceedings of the International Ocean Discovery*
802 *Program, 367/368*. https://doi.org/10.14379/iodp.proc.367368.101.2018
803 Larsen, H. C., Mohn, G., Nirrengarten, M., Sun Z., Stock J., & Jian Z., et al. (2018b). Rapid
804 transition from continental breakup to igneous oceanic crust in the South China Sea. *Nature*
805 *Geoscience, 11*, 782-789. https://doi.org/10.1038/s41561-018-0198-1
806 Lavier, L. L., & Manatschal, G. (2006). A mechanism to thin the continental lithosphere at
807 magma-poor margins. Nature, 440(7082), 324-328. https://doi.org/10.1038/nature04608
808 Lei, C., Alves, T. M., Ren, J., Pang, X., Yang, L. & Liu, J. (2019). Depositional architecture and
809 structural evolution of a region immediately inboard of the locus of continental breakup
810 (Liwan sub-basin, South Shina Sea). *Geological Society of America Bulletin, 131(7-8)*,
811 1059-1074. https://doi.org/10.1130/B35001.1

812 Li, C. F., Xu, X., Lin, J., Sun, Z., & Zhu J., et al. (2014). Ages and magnetic structures of the
813 South China Sea constrained by deep tow magnetic surveys and IODP Expedition 349.
814 *Geochemistry, Geophysics, Geosystems, 15*, 4958-4983.
815 https://doi.org/10.1002/2014GC005567
816 Li, F., Sun, Z., & Yang, H. (2018). Possible spatial distribution of the Mesozoic volcanic arc in
817 the present-day South China Sea continental margin and its tectonic implications. *Journal of*
818 *Geophysical Research: Solid Earth*, 123, 6215-6235. https://doi.org/10.1029/2017JB014861
819 Li, S., Mooney, W. D., & Fan, J. (2006). Crustal structure of mainland China from deep seismic
820 sounding data. *Tectonophysics, 420(1-2)*, 239-252.
821 https://doi.org/10.1016/j.tecto.2006.01.026
822 Li, Z. X., & Li, X. H. (2007). Formation of the 1300-km-wide intracontinental orogen and
823 postorogenic magmatic province in Mesozoic South China: a flat-slab subduction model.
824 *Geology, 35(2)*, 179-182. https://doi.org/10.1130/G23193A.1
825 Lister, G. S., Etheridge, M. A., & Symonds, P. A. (1986). Detachment faulting and the evolution
826 of passive continental margins. *Geology, 14(3)*, 246-250. https://doi.org/10.1130/0091-
827 7613(1986)14<246:DFATEO>2.0.CO;2
828 Lister, G. S., Etheridge, M. A., & Symonds, P. A. (1991). Detachment models for the formation
829 of passive continental margins. *Tectonics, 10(5)*, 1038-1064.
830 https://doi.org/10.1029/90TC01007
831 Liu, S., Zhao, M., Sibuet, J. C., Qiu, X., Wu, J., & Zhang, J., et al. (2018). Geophysical
832 constraints on the lithospheric structure in the northeastern South China Sea and its
833 implications for the South China Sea geodynamics. *Tectonophysics, 742*,101-119.
834 https://doi.org/10.1016/j.tecto.2018.06.002
835 Lizarralde, D., Axen, G., Brown, H., Fletcher, J. & Gonzalez-Fernandez, A., et al. (2007).
836 Variation in styles of rifting in the Gulf of California. *Nature, 448*, 466-469.
837 https://doi.org/10.1038/nature06035
838 Lu, G., & Huismans, R. S. (2021). Melt volume at Atlantic volcanic rifted margins controlled by
839 depth-dependent extension and mantle temperature. *Nature Communications, 12*, 3894.
840 https://doi.org/10.1038/s41467-021-23981-5
841 Manatschal, G., Froitzheim, N., Rubenach, M., & Turrin, B. D. (2001). The role of detachment
842 faulting in the formation of an ocean-continent transition: insights from the Iberia Abyssal

Plain. *Geological Society London Special Publications, 187(1)*, 405-428. https://doi.org/10.1144/GSL.SP.2001.187.01.20

Mckenzie, D. (1978). Some remarks on the development of sedimentary basins. *Earth and Planetary Science Letters, 40(1)*, 25-32. https://doi.org/10.1016/0012-821X(78)90071-7

Minshull, T. A. (2009). Geophysical characterisation of the ocean-continent transition at magma-poor rifted margins. *Comptes Rendus Geoscience, 341(5)*, 382-393. https://doi.org/10.1016/j.crte.2008.09.003

Minshull, T. A., Dean, S. M., White, R. S., & Whitmarsh, R. B. (2001). Anomalous melt production after continental break-up in the southern Iberia Abyssal Plain. *Geological Society London Special Publications, 187(1)*, 537-550. https://doi.org/10.1144/GSL.SP.2001.187.01.26

Nanni, U., Pubellier, M., Chan, L. S., & Sewell, R. J. (2017). Rifting and reactivation of a Cretaceous structural belt at the northern margin of the South China Sea. *Journal of Asian Earth Sciences, 136*, 110-123. https://doi.org/10.1016/j.jseaes.2017.01.008

Nirrengarten M., Mohn G., Kusznir N. J., Sapin F., Despinois F., & Pubellier M., et al. (2020). Extension modes and breakup processes of the southeast China-Northwest Palawan conjugate rifted margins. *Marine and Petroleum Geology, 113*, 104123. https://doi.org/10.1016/j.marpetgeo.2019.104123

Nissen, S. S., Hayes, D. E., Buhl, P., Diebold, J., Bochu, Y., & Zeng, W., et al. (1995a). Deep penetration seismic soundings across the northern margin of the South China Sea. *Journal of Geophysical Research: Solid Earth, 100(B11)*, 22407-22433. https://doi.org/10.1029/95JB01866

Nissen, S. S., Hayes, D. E., Bochu, Y., Zeng, W., Chen, Y., & Nu, X. (1995b), Gravity, heat flow, and seismic constraints on the processes of crustal extension: Northern margin of the South China Sea, *Journal of Geophysical Research: Solid Earth, 100(B11)*, 22447-22483 https://doi.org/10.1029/95JB01868

Paton, D. A., Pindell, J., Mcdermott, K., Bellingham, P., & Horn, B. (2017). Evolution of seaward-dipping reflectors at the onset of oceanic crust formation at volcanic passive margins: insights from the south atlantic. *Geology, 45(5)*, 439-442. https://doi.org/10.1130/G38706.1

873 Perez-Gussiny, M., & Reston, T. J. (2001). Rheological evolution during extension at
874 nonvolcanic rifted margins onset of serpentinization and development of detachments
875 leading to continental breakup. *Journal of Geophysical Research: Solid*
876 *Earth, 106(B3)*, 3961-3975, https://doi.org/10.1029/2000JB900325
877 Peron-Pinvidic, G., & Manatschal, G. (2010). From microcontinents to extensional allochthons:
878 witnesses of how continents rift and break apart?. *Petroleum Geoscience, 16(3)*, 189-197.
879 https://doi.org/10.1016/j.physio.2015.03.3679
880 Peron-Pinvidic, G., Manatschal, G., & Osmundsen, P. T. (2013). Structural comparison of
881 archetypal Atlantic rifted margins: A review of observations and concepts. *Marine and*
882 *Petroleum Geology*, *43*, 21-47. https://doi.org/10.1016/j.marpetgeo.2013.02.002
883 Peron-Pinvidic, G., Manatschal, G., Masini, E., Sutra, E., & Unternehr, P. (2015). Unravelling
884 the along-strike variability of the Angola-Gabon rifted margin: a mapping approach.
885 Geological Society London Special Publications, 438(1). http://doi.org/10.1144/SP438.1
886 Prada, M., Ranero, C. R., Sallares, V., Zitellini, N., & Grevemeyer, I. (2016). Mantle exhumation
887 and sequence of magmatic events in the Magnaghi–Vavilov basin (central Tyrrhenian,
888 Italy): New constraints from geological and geophysical observations. *Tectonophysics, 689*,
889 133-142. https://doi.org/10.1016/j.tecto.2016.01.041
890 Prada, M., Sallares, V., Ranero, C. R., Vendrell, M. G., Grevemeyer, I., & Zitellini, N., et al.
891 (2015). The complex 3-D transition from continental crust to backarc magmatism and
892 exhumed mantle in the Central Tyrrhenian basin. *Geophysical Journal Internationa*l,
893 203(1), 63-78. https://doi.org/10.1093/gji/ggv271
894 Prada, M., Ranero, C.R., Sallares, V., Grevemeyer, I., de Franco, R., Gervasi, A., Zitellini, N.,
895 The structure of Mediterranean arcs: New insights from the Calabrian Arc subduction
896 system, Earth and Planetary Science Letters, vol.548, 116480,
897 https://doi.org/10.1016/j.epsl.2020.116480. 2020
898 Pubellier, M., & Meresse, F. (2013). Phanerozoic growth of Asia: geodynamic processes and
899 evolution. *Journal of Asian earth sciences, 72*, 118-128.
900 https://doi.org/10.1016/j.jseaes.2012.06.013
901 Qiu, X., Ye, S., Wu, S., Shi, X., Zhou, D., & Xia, K., et al. (2001). Crustal structure across the
902 Xisha Trough, northwestern South China Sea. *Tectonophysics, 341(1-4)*, 179-193.
903 https://doi.org/10.1016/S0040-1951(01)00222-0

Ranero, C. R., & Pérez-Gussinyé, M. (2010). Sequential faulting explains the asymmetry and extension discrepancy of conjugate margins. *Nature, 468(7321)*, 294-299. https://doi.org/10.1038/nature09520

Reston, T. J. (2009). The structure, evolution and symmetry of the magma-poor rifted margins of the North and Central Atlantic: A synthesis. *Tectonophysics*, *468*, 6-27. https://doi.org/10.1016/j.tecto.2008.09.002

Sallares, V., Charvis P., Flueh E. R., & Bialas J. (2003). Seismic structure of Cocos and Malpelo Volcanic Ridges and implications for hot spot-ridge interaction, *Journal of Geophysical Research: Solid Earth, 108(B12),* 2564. https://doi.org/10.1029/2003JB002431

Sandwell, D. T., Mueller, R. D., Smith, W. H. F., Garcia, E., & Francis, R. (2014). New global marine gravity model from Cryosat-2 and Jason-1 reveals buried tectonic structure. *Science, 346(6205)*, 65-7. https://doi.org/10.1126/science.1258213

Savva, D., Pubellier, M., Franke, D., Chamot-Rooke, N., Meresse, F., & Steuer, S., et al. (2014). Different expressions of rifting on the South China Sea margins. *Marine and Petroleum Geology, 58*, 579-598. https://doi.org/10.1016/j.marpetgeo.2014.05.023

Shaw, P. R., & Orcutt, J. A. (1985). Waveform inversion of seismic refraction data and applications to young pacific crust. *Geophysical Journal of the Royal Astronomical Society, 82(3)*, 375-414. https://doi.org/10.1111/j.1365-246X.1985.tb05143.x

Stock, J.M., Sun, Z., Klaus, A., Larsen, H.C., Jian, Z., & Alvarez Zarikian, C.A., et al. (2018). Site U1500. *In: Proceedings of the International Ocean Discovery Program, 367/368*. https://doi.org/10.14379/iodp.proc.367368.104.2018

Sun, Z., Lin, J., Qiu, N., Jian, Z., Wang, P. X., & Pang, X., et al. (2019). The role of magmatism in the thinning and breakup of the south china sea continental margin. *National Science Review, 6(5)*, 871-876. https://doi.org/10.1093/nsr/nwz116

Sun, Z., Stock, J., Jian, Z., McIntosh, K., Alvarez Zarikian, C.A., & Klaus, A., 2016. Expedition 367/368 Scientific Prospectus: South China Sea Rifted Margin. *International Ocean Discovery Program*. https://doi.org/10.14379/iodp.sp.367368.2016

Sun, Z., Stock, J.M., Klaus, A., Larsen, H.C., Jian, Z., & Alvarez Zarikian, C.A., et al. (2018). Site U1499. *In: Proceedings of the International Ocean Discovery Program, 367/368*. https://doi.org/10.14379/iodp.proc.367368.103.2018

Sutra, E., & Manatschal, G. (2012). How does the continental crust thin in a hyperextended rifted margin? Insights from the Iberia margin. *Geology, 40(2)*, 139-142. https://doi.org/10.1130/G32786.1

Tatsumi, Y. (2008). Making continental crust: The sanukitoid connection. *Chinese Science Bulletin, 53*, 1620-1633. https://doi.org/10.1007/s11434-008-0185-9

Taylor, B., & Hayes, D. E. (1983). Origin and history of the south China sea basin. *The Tectonic and Geologic Evolution of Southeast Asian Seas and Islands: Part 2*, 23-56.

Tong, C. H., Barton, P. J., White, R. S., Sinha, M. C., Singh, S. C., & Pye, J. W., et al. (2003). Influence of enhanced melt supply on upper crustal structure at a mid-ocean ridge discontinuity: A three-dimensional seismic tomographic study of 9° N East Pacific Rise. *Journal of Geophysical Research: Solid Earth, 108(B10)*, 2464. https://doi.org/10.1029/2002JB002163

Tucholke, B. E., Sawyer, D. S., & Sibuet, J. C. (2007). Breakup of the Newfoundland-Iberia rift. *Geological Society London Special Publications, 282(1)*, 9-46. https://doi.org/10.1144/SP282.2

Vidale, J. (1988). Finite-difference calculation of travel-times. *Bulletin of the Seismological Society of America, 78 (6)*, 2062–2076. https://doi.org/10.1785/BSSA0780062062

Wan, X., Li, C. F., Zhao, M., He, E., Liu, S., Qiu, X., et al (2019). Seismic velocity structure of the magnetic quiet zone and continent-ocean boundary in the northeastern South China Sea. *Journal of Geophysical Research: Solid Earth, 124*, 11866-11899. https://doi.org/10.1029/2019JB017785

Wang, J., Zhao, M., Qiu, X., Sibuet, J. C., He, E., & Zhang, J., et al. (2016). 3D seismic structure of the Zhenbei-Huangyan seamounts chain in the East Sub-basin of the South China Sea and its mechanism of formation. *Geological Journal, 51(S1)*, 448-463. https://doi.org/10.1002/gj.2781

Wang, P., Huang, C. Y., Lin, J., Jian, Z., Sun, Z., & Zhao, M. (2019). The south china sea is not a mini-atlantic: plate-edge rifting vs intra-plate rifting. *National Science Review, 6*, 902-913. https://doi.org/10.1093/nsr/nwz135

Wang, Q., Zhao, M., Zhang, H., Zhang, J., He, E., Yuan, Y., & Qiu, X. (2020). Crustal velocity structure of the Northwest Sub-basin of the South China Sea based on seismic data

964 reprocessing. *Science China Earth Sciences, 63(11)*,1791-
965 806.https://doi.org/10.1007/s11430-020-9654-4
966 Wang, T. K., Chen, M. K., Lee, C. S., & Xia, K. (2006). Seismic imaging of the transitional crust
967 across the northeastern margin of the South China Sea. *Tectonophysics, 412(3-4)*, 237-254.
968 https://doi.org/10.1016/j.tecto.2005.10.039
969 Wei, X., Ruan, A., Zhao, M., Qiu, X., Li, J., & Zhu, J., et al. (2011). A wide-angle OBS profile
970 across Dongsha Uplift and Chaoshan Depression in the mid-northern South China Sea.
971 *Chinese Journal of Geophysics (in Chinese), 2011, 54(12)*, 3325-3335.
972 https://doi.org/10.3969/j.issn.0001-5733.2011.12.030
973 Wernicke, B. (1995). Low-angle normal faults and seismicity: A review. *Journal of Geophysical*
974 *Research: Solid Earth, 100(B10),* 20159-20174. https://doi.org/10.1029/95JB01911
975 Wessel, P., Smith, W. H. F., Scharroo, R., Luis, J., & Wobbe, F. (2013). Generic Mapping Tools:
976 Improved Version Released. *Eos, Transactions American Geophysical Union, 94(45)*, 409–
977 410. https://doi.org/10.1002/2013EO450001
978 White, R. S., Mckenzie, D., & O"Nions, R. K. (1992). Oceanic crustal thickness from seismic
979 measurements and rare earth element inversions. *Journal of Geophysical Research: Solid*
980 *Earth, 97(B13)*, 19683-19715. https://doi.org/10.1029/92JB01749
981 White, R. S., Spence, G. D., Fowler, S. R., Mckenzie, D. P., Westbrook, G. K., & Bowen, A. N.
982 (1987). Magmatism at rifted continental margins. *Nature, 330(6147)*, 439-444.
983 https://doi.org/10.1038/330439a0
984 White, R., & McKenzie, D. (1989). Magmatism at rift zones: the generation of volcanic
985 continental margins and flood basalts. *Journal of Geophysical Research: Solid Earth,*
986 *94(B6),* 7685-7729. https://doi.org/10.1029/JB094iB06p07685
987 Whitmarsh, R. B., Manatschal, G., & Minshull, T. B. (2001). Evolution of magma-poor
988 continental margins from rifting to seafloor spreading. *Nature, 413(6852)*, 150-4.
989 https://doi.org/10.1016/B978-0-444-56357-6.00008-1
990 Whitmarsh, R. B., Manatschal, G., & Minshull, T. B. (2001). Evolution of magma-poor
991 continental margins from rifting to seafloor spreading. *Nature, 413(6852)*, 150-4.
992 https://doi.org/10.1016/B978-0-444-56357-6.00008-1
993 Whitmarsh, R. B., White, R. S., Horsefield, S. J., Sibuet, J.-C., Recq, M., & Louvel,
994 V. (1996). The ocean-continent boundary off the western continental margin of Iberia:

995 Crustal structure west of Galicia Bank. *Journal of Geophysical Research: Solid*
996 *Earth, 101(B12)*, 28291- 28314. https://doi.org/10.1029/96JB02579
997 Wilcock W (2011). Tlpicker users' manual. http://faculty.washington.edu/wilcock/?page_id=39.
998 Yan, P., Hui, D., Liu, H., Zhang, Z., & Jiang, Y. (2006). The temporal and spatial distribution of
999 volcanism in the South China Sea region. *Journal of Asian Earth Sciences, 27(5)*, 647-659.
1000 https://doi.org/10.1016/j.jseaes.2005.06.005
1001 Yan, P., Zhou, D., & Liu, Z. (2001). A crustal structure profile across the northern continental
1002 margin of the south china sea. *Tectonophysics, 338(1)*, 1-21. https://doi.org/10.1016/S0040-
1003 1951(01)00062-2
1004 Yang, F., Zhang, J., Du, F., Wang, Q., Pang, X., Zhao, M., & Qiu, X. (2020). A new method for
1005 shots and OBSs' relocation applying in three-dimensional seismic survey. *Chinese Journal*
1006 *of Geophysics (in Chinese), 63(2)*, 766-777. https://doi.org/10.6038/cjg2020N0150
1007 Yang, L., Ren, J., McIntosh, K., Pang, X., Lei, C., & Zhao, Y. (2018). The structure and
1008 evolution of deepwater basins in the distal margin of the northern South China Sea and their
1009 implications for the formation of the continental margin. *Marine and Petroleum Geology,*
1010 *92*, 234-254. https://doi.org/10.1016/j.marpetgeo.2018.02.032
1011 Ye, Q., Mei, L., Shi, H., Camanni, G., Shu, Y., & Wu, J., et al. (2018). The late cretaceous
1012 tectonic evolution of the South China Sea area: an overview, and new perspectives from 3D
1013 seismic reflection data. *Earth-Science Reviews, 187*, 186-204.
1014 https://doi.org/10.1016/j.earscirev.2018.09.013
1015 Zelt, C. A., & Barton, P. J. (1998). Three-dimensional seismic refraction tomography: a
1016 comparison of two methods applied to data from the faeroe basin. *Journal of Geophysical*
1017 *Research: Solid Earth, 103(B4)*, 7187-7210. https://doi.org/10.1029/97JB03536
1018 Zelt, C. A., & Smith, R. B. (1992). Seismic travel-time inversion for 2-D crustal velocity
1019 structure. *Geophysical Journal International, 108(1)*, 16-34. https://doi.org/10.1111/j.1365-
1020 246X.1992.tb00836.x
1021 Zelt, C., A., & Forsyth, D. A. (1994). Modeling wide-angle seismic data for crustal structure:
1022 southeastern Grenville province. *Journal of Geophysical Research: Solid Earth, 99(B6)*,
1023 11687-11704. https://doi.org/10.1029/93JB02764
1024 Zhang, C., Manatschal, G., Pang, X., Sun, Z., & Zheng, J., et al. (2020). Discovery of mega-
1025 sheath folds flooring the Liwan subbasin (South China Sea): implications for the rheology

of hyperextended crust. *Geochemistry, Geophysics, Geosystems, 21(7)*, e2020GC009023. https://doi.org/10.1029/2020GC009023

Zhang, C., Sun, Z., Manatschal, G., Pang, X., & Zhao, M. (2021). Ocean-continent transition architecture and breakup mechanism at the mid-northern South China Sea. *Earth-Science Reviews, 217*, 103620. https://doi.org/10.1016/j.earscirev.2021.103620

Zhang, J., Zhao M., & Qiu, X. (2022). Ocean Bottom Seismometer data of a three-dimensional seismic survey in the northern South China Sea distal margin [Dataset]. Science Data Bank. https://www.scidb.cn/anonymous/ckVyTVpm

Zhao, F., Alves, T. M., Xia, S., Li, W., & Fan, C. (2019). Along-strike segmentation of the South China Sea margin imposed by inherited pre-rift basement structures. *Earth and Planetary Science Letters, 530*, 115862. https://doi.org/10.1016/j.epsl.2019.115862

Zhao, M., Qiu, X., Li, J., Sauter, D., Ruan, A., & Chen, J., et al. (2013). Three-dimensional seismic structure of the Dragon Flag oceanic core complex at the ultraslow spreading Southwest Indian Ridge (49°39′ E). *Geochemistry Geophysics Geosystems, 14(10)*, 4544-4563. https://doi.org/10.1002/ggge.20264

Zhou, D., Wang, W., Wang, J., Pang, X., Cai D. & Sun Z. (2006). Mesozoic subduction-accretion zone in northeastern South China Sea inferred from geophysical interpretations. *Science in China Series D Earth Sciences, 49(5)*, 471-482. https://doi.org/10.1007/s11430-006-0471-9